Two-Dimensional Multiple-Quantum MAS NMR of Quadrupolar Nuclei: A Comparison of Methods

Steven P. Brown and Stephen Wimperis

Physical Chemistry Laboratory, University of Oxford, South Parks Road, Oxford OX1 3QZ, United Kingdom

Multiple-quantum magic-angle-spinning (MQMAS) NMR experiments have recently been used to remove second-order broadening from the central transition of half-integer quadrupolar nuclei. In this paper, the various methods that have been proposed for obtaining pure absorption-mode lineshapes in MQMAS experiments are described and compared. The methods can be classified according to whether the data are amplitude- or phase-modulated as a function of the evolution period, t_1. Both classes of experiment are usually performed in such a way that the inhomogeneous quadrupolar broadening is spread out along a ridge which, for spins $I = 3/2$ and $5/2$, respectively, has a slope of $-7/9$ or $19/12$ with respect to the F_2 axis. This paper shows, however, that there are disadvantages associated with recording the data in this fashion and demonstrates, in particular, that a shearing transformation of the final two-dimensional spectrum can lead to distorted lineshapes. Novel amplitude- and phase-modulated "split-t_1" MQMAS experiments are introduced which fully refocus the second-order broadening during the evolution period, t_1, thereby avoiding the need for a shearing transformation. The considerable practical advantages of these split-t_1 experiments are discussed, particularly with regard to ease of implementation and processing. In general, the sensitivities achievable using the split-t_1 MQMAS experiments are predicted to be similar to those obtainable with other methods and, in the special case of the spin $I = 3/2$ phase-modulated experiments, are even shown to be slightly superior. © 1997 Academic Press

INTRODUCTION

Recently, much interest has focused on the realization that inhomogeneous second-order quadrupolar broadening can be removed from the NMR spectra of half-integer quadrupolar nuclei by correlating multiple- and single-quantum coherences in the presence of magic-angle spinning (MAS) (*1–25*). While MAS is routinely used to narrow lines that are broadened to first order (*26*), it has been known for many years that rotation around a single axis can only partially remove the second-order quadrupolar broadening associated with the central transition of half-integer quadrupolar nuclei (*27*). Although the ability of double rotation (DOR) and dynamic-angle-spinning (DAS) techniques to remove this broadening has been successfully demonstrated (*28–31*), the technical complexity of such experiments has meant that

their use has not become widespread. In 1995, Frydman and Harwood demonstrated that sample rotation about two different angles (as in both DOR and DAS) is not necessary to remove the second-order quadrupolar broadening, since the required second degree of freedom can be introduced by performing a two-dimensional experiment in which multiple- and single-quantum coherences are correlated (*1*).

In the original multiple-quantum magic-angle-spinning (MQMAS) experiment of Frydman and Harwood (*1*), phase cycling is used to select a coherence transfer pathway which gives rise to two-dimensional ''phase-twist'' lineshapes. Recent work, however, has shown that the original experiment can easily be modified to ensure that pure absorption-mode lineshapes are obtained (*2–5, 10*). These modified experiments are of two distinct types. In the first type, the echo and antiecho pathways are combined with equal amplitude to yield a signal which is *amplitude-modulated* with respect to t_1; a ''hypercomplex'' two-dimensional Fourier transform then gives rise to pure absorption-mode lineshapes (*2–5, 10*). In the second type, only one pathway is selected and the signal is *phase-modulated* with respect to t_1. Normally, phase modulation gives rise to two-dimensional phase-twist lineshapes, as in the original experiment of Frydman and Harwood. If, however, the inhomogeneous quadrupolar broadening dominates the homogeneous broadening (which is often the case with samples for which the MQMAS technique is applicable), pure absorption-mode lineshapes can still be obtained through acquisition of the whole echo (*4*).

In the simplest amplitude-modulated experiment (the theory of which is presented later), the inhomogeneous quadrupolar broadening is spread out along a ''ridge'' (*32*) which, for $I = 3/2$ nuclei, has a slope of $-7/9$ with respect to the F_2 axis. A spectrum displaying only isotropic shifts (both chemical and second-order quadrupolar in origin) can then be obtained by calculating the projection of the two-dimensional spectrum onto an axis orthogonal to the ridges. In practice, such a projection is more easily obtained by first performing a shearing transformation such that the ridges appear parallel to the F_2 axis. Recently, we have demonstrated experiments in which both triple- and single-quantum evolution occurs during t_1, with the result that the anisotropic

second-order quadrupolar broadening is fully refocused in t_1 and, hence, the inhomogeneously broadened ridges appear parallel to the F_2 axis without the need for any shearing transformation (*10, 25*).

The purpose of this paper is to discuss the advantages of these ''split-t_1'' experiments and, in particular, to compare them with other methods for obtaining pure absorption-mode lineshapes in the MQMAS experiment.

QUADRUPOLAR BROADENING

The splitting of the energy levels by the quadrupolar interaction can be calculated using time-independent perturbation or average Hamiltonian theory. This calculation has been presented in detail elsewhere and will not be repeated here (*10, 29, 33*). An important result is that the $|m_I = +s\rangle \leftrightarrow |m_I = -s\rangle$ transitions are not broadened by the quadrupolar coupling to first order. A consequence of this is the well-known fact that if the quadrupolar frequency, ω_Q^{PAS} (the superscript PAS refers to the principal axis system of the quadrupolar interaction), is large then only the central transition, $|m_I = \frac{1}{2}\rangle \leftrightarrow |m_I = -\frac{1}{2}\rangle$, is observed in the normal spectrum. However, when ω_Q^{PAS} is so large that it is of comparable magnitude to the Larmor frequency, ω_0, it becomes necessary to include a second-order approximation and this now reveals a broadening of the $|m_I = +s\rangle \leftrightarrow |m_I = -s\rangle$ transitions by the quadrupolar coupling. Over an integral number of sample spinning periods at an angle χ between the spinning axis and the z axis of the laboratory frame, the average second-order frequency shift for a half-integer quadrupolar spin, I, is given by

$$\langle E_{|s\rangle}^{(2)} - E_{|-s\rangle}^{(2)} \rangle$$

$$= \frac{(\omega_Q^{PAS})^2}{\omega_0} \{ A_s^I Q^0(\eta) + B_s^I d_{0,0}^2(\chi) Q^2(\alpha, \beta, \eta)$$

$$+ C_s^I d_{0,0}^4(\chi) Q^4(\alpha, \beta, \eta) \}. \qquad [1]$$

The quadrupolar frequency, ω_Q^{PAS}, is defined such that, to first order, the satellite transitions, for $I = 3/2$ nuclei, appear at $\omega_0 \pm 2\omega_Q$, i.e.,

$$\omega_Q^{PAS} = \frac{3\pi C_Q}{2I(2I - 1)}, \qquad [2a]$$

$$\omega_Q = \frac{\omega_Q^{PAS}}{2} (3\cos^2\theta - 1 + \eta \sin^2\theta \cos 2\phi), \qquad [2b]$$

where the angles θ and ϕ describe the rotation of the principal axis system of the quadrupolar interaction onto the laboratory frame and where C_Q, the quadrupolar coupling constant, is in units of hertz and is given by

$$C_Q = \frac{e^2 qQ}{h}. \qquad [2c]$$

TABLE 1
Coefficients of the Zero-, Second-, and Fourth-Rank Contributions to the Second-Order Frequency Shift, given in Eq. [1]

I	s	A_s^I	B_s^I	C_s^I
3/2	1/2	−2/5	−8/7	54/35
3/2	3/2	6/5	0	−6/5
5/2	1/2	−16/15	−64/21	144/35
5/2	3/2	−4/5	−40/7	228/35
5/2	5/2	20/3	40/21	−60/7

The functions $Q^0(\eta)$ and $Q^l(\alpha, \beta, \eta)$, where η corresponds to the asymmetry parameter and the angles α and β describe the rotation of the principal axis system of the quadrupolar interaction onto the sample frame, are given explicitly by

$$Q^0(\eta) = \left(1 + \frac{\eta^2}{3}\right) \qquad [3a]$$

$$Q^2(\alpha, \beta, \eta) = \left(1 - \frac{\eta^2}{3}\right) d_{0,0}^2(\beta) - \frac{\sqrt{8}}{\sqrt{3}} \eta d_{2,0}^2(\beta) \cos 2\alpha \qquad [3b]$$

$$Q^4(\alpha, \beta, \eta) = \left(1 + \frac{\eta^2}{18}\right) d_{0,0}^4(\beta)$$

$$+ \frac{\sqrt{10}}{3} \eta d_{2,0}^4(\beta) \cos 2\alpha$$

$$+ \frac{35}{9\sqrt{70}} \eta^2 d_{4,0}^4(\beta) \cos 4\alpha, \qquad [3c]$$

where the $d_{m',m}^l(\beta)$ terms are reduced Wigner matrix elements (*34*). The coefficients A_s^I, B_s^I, and C_s^I are given in Table 1 for spins $I = 3/2$ and $5/2$. Thus, for a single crystallite spinning about an axis χ, there is an isotropic frequency shift of the central transition of $A_s^I Q^0(\eta)(\omega_Q^{PAS})^2/\omega_0$, as well as rank $l = 2$ and $l = 4$ anisotropic shifts with amplitudes that depend on the angles χ, α, and β. In a powdered sample, a spherical average over all orientations of the angles α and β must be considered and gives rise to rank $l = 2$ and $l = 4$ inhomogeneous broadening.

To obtain an informative high-resolution spectrum, it is necessary to remove the anisotropic shifts, while retaining the isotropic shifts. Since the two $d_{0,0}^l(\chi)$ terms do not have a common root, spinning around a unique angle χ cannot remove both rank $l = 2$ and $l = 4$ anisotropic broadenings. For example, spinning at the magic angle will completely remove rank $l = 2$ broadening, since $d_{0,0}^2(54.7°) = 0$, but only partially average rank $l = 4$ broadening. The major contribution of Frydman and Harwood was to recognize that the coefficients of the isotropic and anisotropic shifts differ between single- and multiple-quantum transitions (*1*). The rank $l = 4$ anisotropic broad-
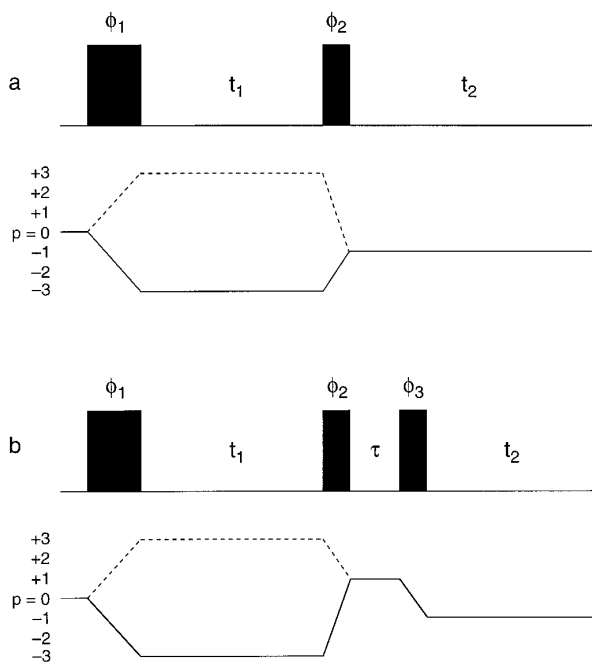
FIG. 1. Pulse sequences and coherence transfer pathway diagrams for the (a) simple echo (solid line) and simple antiecho (dashed line) and (b) shifted-echo (solid line) and shifted-antiecho (dashed line) MQMAS experiments (for spin $I = 3/2$ nuclei). Amplitude-modulated experiments result if both the echo and the antiecho pathways are retained and have equal amplitudes. The optimum flip angles for the individual pulses are described in the text. The spin-echo interval, τ, in (b) should be chosen to ensure that a whole echo is obtained in t_2 for all values of t_1. Phase cycling schemes for the pulse phases ϕ_1, ϕ_2, and ϕ_3 and for the receiver R_x are given in Tables A1 and A2 of the Appendix.

ening can hence be refocused, while still retaining the isotropic information, by performing a two-dimensional experiment in which multiple- and single-quantum coherences are correlated, while spinning at the magic angle to remove rank $l = 2$ anisotropic broadening. Spinning at the magic angle has the advantages that (i) conventional MAS hardware can be used and (ii) MAS will also average any additional first-order broadening due to dipolar couplings or CSA. Although the technique is applicable to quintuple- and higher-quantum coherences (*3, 8, 23*), for brevity, discussion in this paper will be restricted to experiments involving triple- and single-quantum coherences.

The ratio of the rank $l = 4$ anisotropic broadening between triple- and single-quantum coherences is of such significance in these experiments that it will be referred to as the MQMAS ratio. For spin $I = 3/2$ and $5/2$, the MQMAS ratio equals $-7/9$ and $19/12$, respectively. It is important to note the difference in sign in the MQMAS ratio between $I = 3/2$ and $5/2$ nuclei. As will become clearer in the following section, this has significant consequences with respect to coherence transfer pathway selection. Therefore, for clarity, the discussion in the main part of the paper will be restricted to spin $I = 3/2$, with the spin $I = 5/2$ case being considered in the final section.

ECHOES, ANTIECHOES, AND SHIFTED ECHOES

Figure 1a shows the pulse sequence and coherence transfer pathway diagram (*35*) corresponding to the original experiment of Frydman and Harwood (*1*). (Frydman and Harwood initially used a two-pulse sequence for excitation of multiple-quantum coherence (*1*), but it has subsequently been shown that single-pulse excitation (*36, 37*) is more efficient (*2–6, 10*).) The sign of the MQMAS ratio is very important since it determines the relative sign of triple- and single-quantum coherences necessary to refocus the second-order broadening and form an echo. Thus, for spin $I = 3/2$ nuclei, since the MQMAS ratio is negative, the *echo pathway* corresponds to the correlation of $p = -3$ and $p = -1$ coherences (solid line in Fig. 1a). The key feature of this and all MQMAS experiments is that the rank $l = 4$ anisotropic broadening is refocused when the ratio of the durations of the single- and triple-quantum coherence evolution periods equals the magnitude of the MQMAS ratio.

In describing MQMAS experiments, it is also useful to introduce the concept of an *antiecho pathway,* where the rank $l = 4$ anisotropic broadening appears to be refocused at negative values of the acquisition time, t_2. The antiecho pathway corresponds to the dashed line in Fig. 1a. Figures 2a and 2b show schematic representations of the time-domain data sets obtained for experiments that select the echo and antiecho pathways, respectively. When $t_1 = 0$, a half echo (i.e., the signal falls from its maximum value to zero) forms at $t_2 = 0$ for both pulse sequences. As t_1 increases, the echo tracks forward and backward through t_2 for the echo
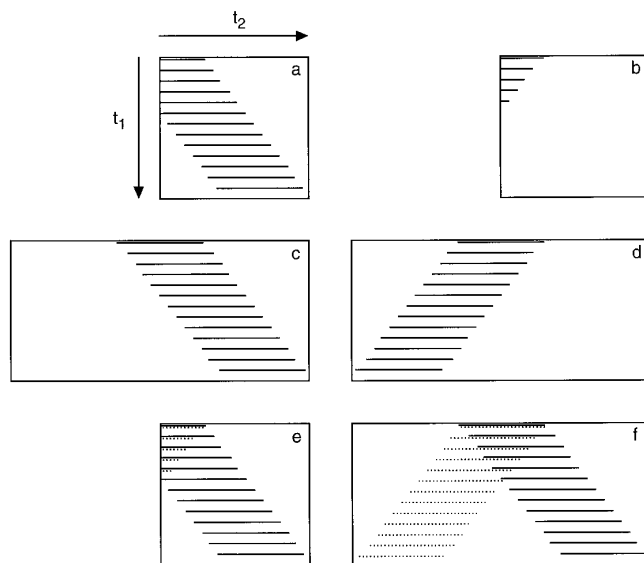
FIG. 2. Schematic representations of the spin $I = 3/2$ time-domain signal obtained with the (a) simple echo, (b) simple antiecho, (c) shifted-echo, (d) shifted-antiecho, (e) simple amplitude-modulated, and (f) amplitude-modulated whole-echo experiments. In (e) and (f), the contributions of the echo and antiecho pathways are shown as solid and dotted lines, respectively.

and antiecho sequences, respectively. Eventually a point is reached where, while there is a whole echo (i.e., the signal starts from zero, rises to its maximum value, and then returns to zero) in Fig. 2a, the signal has disappeared outside the acquisition window in Fig. 2b.

Extending methods developed for the DAS technique (31), Massiot *et al.* have recently presented MQMAS experiments in which the signals from the echo and antiecho experiments are *shifted* in t_2 by forming a spin echo using a selective inversion pulse on the central transition (4). The shifted-echo (solid line) and shifted-antiecho (dashed line) coherence transfer pathways are shown in Fig. 1b. Figures 2c and 2d show schematic representations of the time-domain data sets obtained for the shifted-echo and shifted-antiecho experiments, respectively. As in Figs. 2a and 2b, the echo still moves forward and backward, respectively, in t_2 as t_1 increases but there are now two important differences. Provided that the spin-echo interval, τ, is of sufficient length, first, at $t_1 = 0$, a whole, rather than half, echo is formed and, second, the antiecho signal does not disappear from the acquisition window as t_1 increases. Since whole echoes are obtained for all values of t_1, experiments based on shifted-echo and shifted-antiecho sequences are referred to as *whole-echo* experiments.

The remainder of this paper will describe how the simple echo, simple antiecho, shifted-echo, and shifted-antiecho pulse sequences are used to yield pure absorption-mode two-dimensional lineshapes. The discussion will further describe how the experiments can be easily modified to allow both triple- and single-quantum evolution during t_1, such that a shearing transformation is no longer required.

EXPERIMENTAL AND SIMULATION DETAILS

Experimental NMR spectra presented in this paper were obtained on Bruker MSL 400 and AC 300 spectrometers, equipped with 9.4 T wide-bore and 7.05 T standard-bore magnets, respectively. Experiments on the MSL 400 used a 1 kW radiofrequency amplifier designed for NMR of solid samples, while the AC 300 used a 300 W radiofrequency amplifier intended for NMR of liquid samples. Unless otherwise stated, maximum radiofrequency power was used for all pulses. The following samples were studied: (i) rubidium nitrate, $RbNO_3$, for ^{87}Rb ($I = 3/2$) NMR at 130.9 MHz (MSL 400) and at 98.2 MHz (AC 300); (ii) dibasic sodium phosphate, Na_2HPO_4, for ^{23}Na ($I = 3/2$) NMR at 105.8 MHz (MSL 400); (iii) an approximately equal mixture of sodium oxalate, $Na_2C_2O_4$, and sodium sulfate, Na_2SO_4, for ^{23}Na NMR at 105.8 MHz (MSL 400); and (iv) the mineral kyanite, Al_2SiO_5, for ^{27}Al ($I = 5/2$) NMR at 104.2 MHz (MSL 400). These model samples were chosen because they yield favorable signal-to-noise ratios and have short T_1 relaxation times. Samples (i), (ii), and (iii) were packed in 7 mm MAS rotors and spun at speeds of approximately 5 kHz, while sample (iv) was packed in a 4 mm MAS rotor and spun at approximately 8.5 kHz.

In all experiments, a single long pulse was used to excite triple-quantum coherence. The duration of this pulse was optimized experimentally, either simply to maximize the amount of triple-quantum coherence excited (5, 12) or, with the aim of reducing the level of unwanted artifacts in the final two-dimensional spectrum, to do so within the constraint that the amount of single-quantum coherence generated should be minimized (4, 10). In experiments containing spin echoes, the spin-echo interval was set equal to an integral number of rotor periods (4, 14). The phase cycling used for each different pulse sequence is described in the Appendix. Other experimental details are given in the figure legends and in the text. The results were processed offline using software written in Oxford by Paul Hodgkinson. In contour plots, positive and negative contours are shown as solid and dashed lines, and, except where otherwise stated, contour levels correspond to 4, 8, 16, 32, and 64% of the maximum peak height.

All computer simulations were performed in the time domain, using an explicit density matrix calculation. The contribution of the second-order quadrupolar splitting was included, with the following assumptions being made. For the pulse Hamiltonian, the sample was considered to be stationary (5) for the duration of the pulse (typical pulse lengths are of the order of 5 μs, while the rotor periods are about 200 μs) while, for the free precession Hamiltonian, Eq. [1] was assumed to be valid. The asymmetry parameter, η, was set equal to zero, such that it was necessary to average only over one angle, β, during a free precession period and over two angles, β and the initial rotor phase, during a pulse.

PURE ABSORPTION-MODE TWO-DIMENSIONAL LINESHAPES

In the original experiment of Frydman and Harwood (1) (Fig. 1a), phase cycling is used to select a pathway which is phase-modulated with respect to t_1. Using Eq. [1], the time-domain signal, in the presence of MAS and neglecting homogeneous broadening and chemical shift terms, is given by

$$s(t_1, t_2) = \exp\left\{ -i \frac{(\omega_Q^{PAS})^2}{\omega_0} \left[\frac{6}{5} Q^0(\eta) \right. \right.$$
$$\left. - \frac{6}{5} d_{0,0}^4(\chi) Q^4(\alpha, \beta, \eta) \right] t_1 \right\}$$
$$\times \exp\left\{ -i \frac{(\omega_Q^{PAS})^2}{\omega_0} \left[- \frac{2}{5} Q^0(\eta) \right. \right.$$
$$\left. + \frac{54}{35} d_{0,0}^4(\chi) Q^4(\alpha, \beta, \eta) \right] t_2 \right\}. \quad [4]$$

It is well known that the complex two-dimensional Fourier transform of a time-domain data set of the type $\exp\{iAt_1\}\exp\{iBt_2\}$ gives rise to undesirable two-dimensional phase-twist lineshapes (38). Figures 3a and 3b show simulated
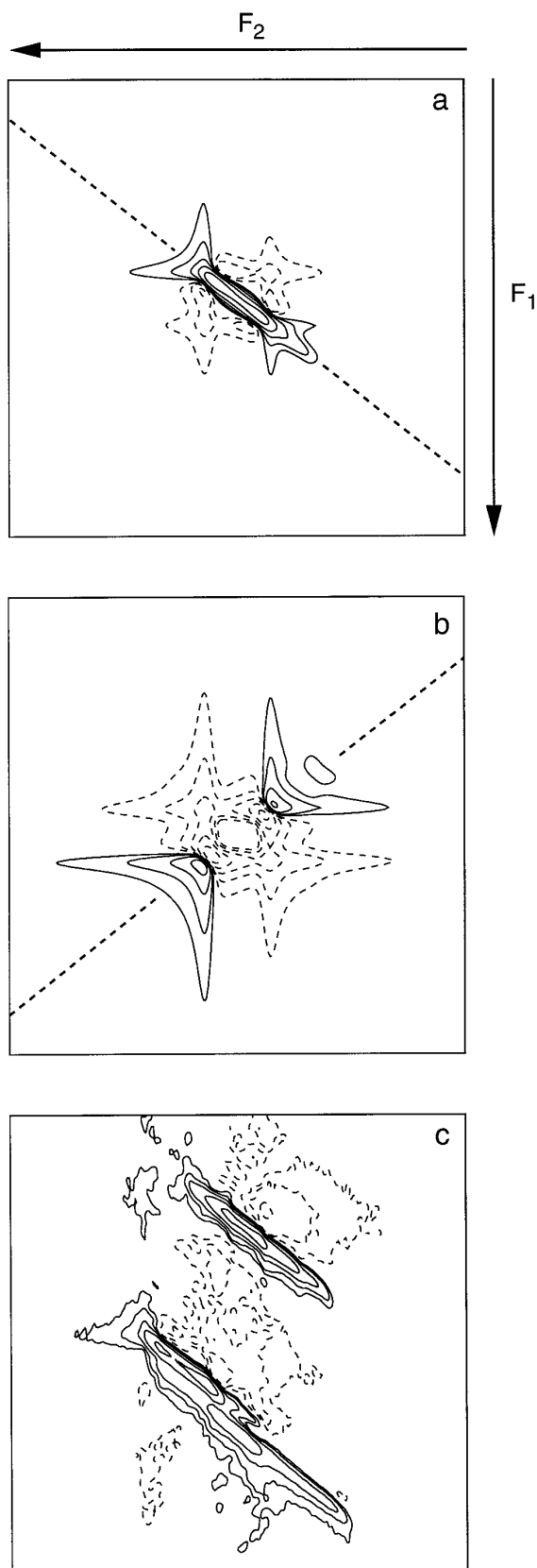
FIG. 3. Contour plots of spin $I = 3/2$ spectra obtained with the simple echo (a) and (c) and simple antiecho (b) experiments in Fig. 1a. The

spectra for the simple echo and simple antiecho experiments, respectively. In both cases, the presence of the rank $l = 4$ anisotropic broadening means that the phase-twist lineshapes add up to form a ridge. However, while, for the echo sequence, the phase-twist lineshapes add up constructively with the gradient of the ridge (with respect to the F_2 axis) equaling the MQMAS ratio, for the antiecho sequence the gradient has the opposite sign to the MQMAS ratio and the phase-twist lineshapes add up destructively. The consequences of the constructive and destructive summation of lineshapes are evident in Figs. 3a and 3b; in particular, the dispersive character is less apparent in the echo pathway lineshape, especially at the center of the ridge (*38*). In addition, it should be noted that the signal maximum in Fig. 3a is twice that in Fig. 3b, which is unsurprising if the time-domain representations shown in Figs. 2a and 2b are compared.

Figure 3c shows a ^{87}Rb spectrum of RbNO$_3$ obtained with the simple echo sequence in Fig. 1a. The spectrum contains three ridges corresponding to the three Rb sites in the unit cell (the lower two ridges are only partially separated). The obvious dispersive character of the phase-twist lineshapes reduces the degree to which different sites are resolved, and it is, therefore, much better to obtain pure absorption-mode two-dimensional lineshapes. The next three subsections discuss methods for obtaining such lineshapes.

The Simple Amplitude-Modulated Experiment

If the echo and antiecho pathways in Fig. 1a are combined with the same amplitude, an amplitude-modulated signal is obtained as a function of t_1 (*38*). In the case where the two pathways add, the signal is cosine-modulated:

$$s(t_1, t_2) = 2 \cos\left\{ \frac{(\omega_Q^{PAS})^2}{\omega_0} \left[\frac{6}{5} Q^0(\eta) \right.\right.$$
$$\left. - \frac{6}{5} d_{0,0}^4(\chi) Q^4(\alpha, \beta, \eta) \right] t_1 \right\}$$
$$\times \exp\left\{ -i \frac{(\omega_Q^{PAS})^2}{\omega_0} \left[-\frac{2}{5} Q^0(\eta) \right.\right.$$
$$\left.\left. + \frac{54}{35} d_{0,0}^4(\chi) Q^4(\alpha, \beta, \eta) \right] t_2 \right\}. \quad [5]$$

A schematic representation of this time-domain data set is

spectra in (a) and (b) were simulated in the time domain and it can be seen that phase-twist lineshapes add up to form a ridge, as indicated by the dashed line. The contour plot in (c) corresponds to a 5×5 kHz region of a ^{87}Rb NMR (130.9 MHz) spectrum of RbNO$_3$. The full F_1 and F_2 spectral widths were 25 and 17.2 kHz, respectively; 96 transients (consisting of 512 points each) were averaged for each of 128 increments of t_1; and the relaxation interval was 100 ms. The durations of the triple-quantum excitation and the $p = -3$ to $p = -1$ reconversion pulses were 6.8 and 2.4 μs, respectively.

given in Fig. 2e, with the contributions of the echo and antiecho pathways being shown as solid and dashed lines, respectively. Pure absorption-mode lineshapes are obtained in the frequency-domain spectrum if a hypercomplex two-dimensional Fourier transform is performed. (A hypercomplex two-dimensional Fourier transform differs from a complex two-dimensional transform in that, in the former, the real and imaginary parts of the data are separated after the first Fourier transform with respect to t_2 and then transformed individually with respect to t_1 (38).)

One disadvantage of acquiring and processing amplitude-modulated data in this way is that it is not possible to discriminate the sign of the multiple-quantum coherences evolving in t_1; i.e., the hypercomplex two-dimensional Fourier transform gives a spectrum which is symmetrical about $F_1 = 0$. Sign discrimination can, however, be easily restored using the States–Haberkorn–Ruben method (39) (or TPPI (40), if real Fourier transforms are used), which in this case, since $p = +3$ and -3 coherences are excited by the first pulse, involves changing the phase of the first pulse by 30°, such that separate cosine- and sine-modulated data sets are recorded.

Phase-Modulated Whole-Echo Experiments

The pulse sequence and coherence transfer pathway diagram for the shifted-echo experiment was shown in Fig. 1b. This experiment differs from the simple echo experiment only in the presence of a spin echo, and the time-domain signal is now given by

$$s(t_1, t_2) = \exp\left\{ -i\frac{(\omega_Q^{PAS})^2}{\omega_0}\left[\frac{6}{5}Q^0(\eta)\right.\right.$$
$$\left.\left. -\frac{6}{5}d_{0,0}^4(\chi)Q^4(\alpha,\beta,\eta)\right]t_1\right\}$$
$$\times \exp\left\{ -i\frac{(\omega_Q^{PAS})^2}{\omega_0}\left[-\frac{2}{5}Q^0(\eta)\right.\right.$$
$$\left.\left. +\frac{54}{35}d_{0,0}^4(\chi)Q^4(\alpha,\beta,\eta)\right](t_2-\tau)\right\}, \quad [6]$$

where τ is the length of the spin-echo interval. From Eq. [6], it can be seen that the $l = 4$ anisotropic frequency shifts are refocused when

$$t_2 = \tau + \tfrac{6}{5}\left(\tfrac{35}{54}\right)t_1 = \tau + \tfrac{7}{9}t_1. \quad [7]$$

An expression analogous to Eq. [6] can easily be obtained for the shifted-antiecho experiment, and it is found that refocusing now occurs when

$$t_2 = \tau - \tfrac{7}{9}t_1. \quad [8]$$

Thus, as demonstrated in Figs. 2c and 2d, as t_1 increases, the echo moves forward and backward in t_2 for the shifted-echo and shifted-antiecho experiments, respectively. In practice, this has the obvious consequence that the τ interval must be significantly longer in the shifted-antiecho experiment; hence there is more signal loss through relaxation than in the shifted-echo experiment. For the shifted-echo experiment, the τ period can be kept to a minimum, since it only needs to be of sufficient length to ensure that the echo is not truncated.

The difference in the direction in which the echo moves as t_1 is incremented might also be expected to have an effect on the resolution of the isotropic projection. The expressions given so far for the time-domain signal have neglected the effect of relaxation. To include the effect of transverse relaxation in the expression for the shifted-echo experiment, given in Eq. [6], it is necessary to multiply by an additional factor of

$$\exp\{-R^{TQ}t_1\}\exp\{-R^{SQ}(\tau + t_2)\}, \quad [9]$$

where R^{TQ} and R^{SQ} correspond to the relaxation rates of triple- and single-quantum coherence. The effect of relaxation on the shifted-antiecho experiment is also given by Eq. [9], except that, as discussed above, the τ interval will be much longer. Considering only the point at which refocusing occurs, substituting the expressions for t_2 in Eqs. [7] and [8] into Eq. [9] yields

$$\exp\{-(R^{TQ} \pm \tfrac{7}{9}R^{SQ})t_1\}\exp\{-2R^{SQ}\tau\}, \quad [10]$$

where the + or − sign refers to the shifted-echo and shifted-antiecho experiments, respectively. Equation [10] describes the decay due to transverse relaxation of the time-domain counterpart of the projection of the two-dimensional spectrum onto an axis orthogonal to the ridges. Unless R^{SQ} is significantly less than R^{TQ}, it would, therefore, be expected that relaxation is slower, and, hence, the resolution in the isotropic projection is better for the shifted-antiecho experiment. However, to date, we have found no convincing experimental evidence for a difference in resolution between the shifted-echo and shifted-antiecho experiments.

The success of these experiments, with regard to obtaining pure absorption-mode two-dimensional lineshapes, depends on the properties of whole echoes. A principle much used in magnetic resonance imaging (41) is that the complex one-dimensional Fourier transform of a function whose real and imaginary parts are respectively symmetric and anti-symmetric around $t = 0$ yields a spectrum whose real part is purely absorptive and whose imaginary part is zero. This is illustrated in Fig. 4a. In the shifted-echo and shifted-antiecho MQMAS experiments, to obtain such a symmetric function, it is essential that the inhomogeneous second-order quadrupolar broadening dominate the homogeneous (i.e., that due
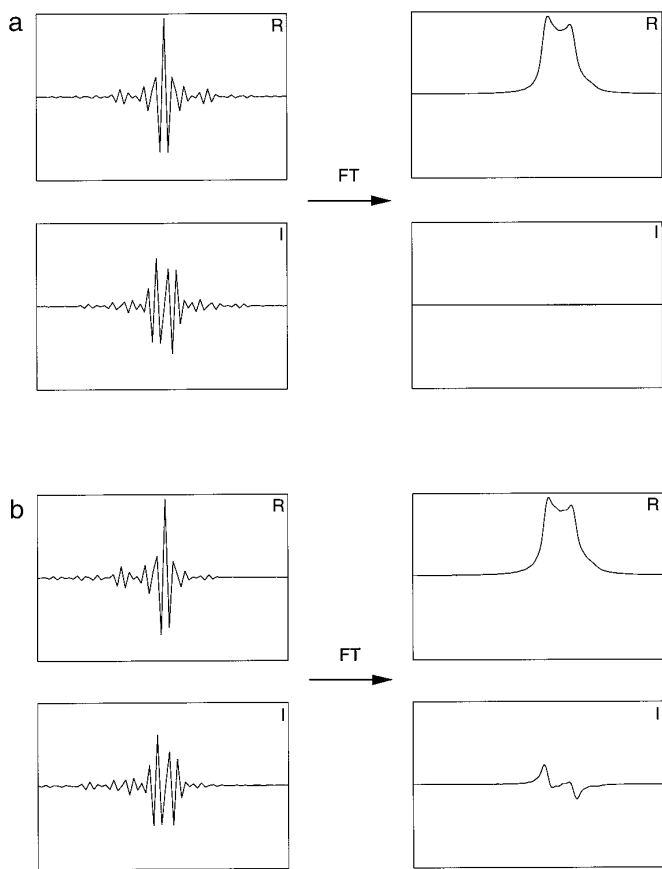
FIG. 4. (a) The complex Fourier transform of a simulated time-domain signal whose real and imaginary parts are symmetric and antisymmetric about $t = 0$, respectively, gives rise to a frequency-domain signal whose real part is purely absorptive and whose imaginary part is zero. (b) When the symmetry of the echo is lost (in this case, due to the application of an exponential damping function to mimic the effects of relaxation), the imaginary part is no longer zero, but now contains a dispersive contribution.

to transverse relaxation) broadening (*4*). When the homogeneous broadening becomes significant, the symmetry of the echo is lost. In such a situation, as shown in Fig. 4b, the imaginary part of the spectrum now contains a dispersive contribution.

Experimentally, since the echo forms at $t_2 = \tau$, rather than $t_2 = 0$, when $t_1 = 0$, it is necessary to apply a τ-dependent first-order phase correction equal to $\exp\{i\omega_2\tau\}$ (*4*). If the echo forms at the center of t_2, the application of this phase correction becomes considerably easier. As shown in Fig. 2 of Ref. (*25*), such a phase correction corresponds to simply either shifting the time origin of the Fourier transform to the center of the echo (the method adopted in this paper), or, in frequency domain, negating alternate data points (*42*).

The properties of whole echoes, therefore, mean that, even though the time-domain signal in Eq. [6] is phase-modulated with respect to t_1, as in the original experiment of Frydman and Harwood (*1*), a complex two-dimensional Fourier transform gives rise to pure absorption-mode lineshapes, provided

that the inhomogeneous broadening dominates the homogeneous broadening. Furthermore, the selection of phase modulation intrinsically yields sign discrimination in F_1.

The Amplitude-Modulated Whole-Echo Experiment

Massiot *et al.* have also presented an amplitude-modulated whole-echo experiment (*4*), which is simply a combination of the shifted-echo and shifted-antiecho sequences of Fig. 1b. A schematic time-domain data set for the experiment is shown in Fig. 2f, with the contributions of the shifted-echo and shifted-antiecho pathways again being shown as solid and dashed lines respectively. As with the phase-modulated whole-echo experiment, pure absorption-mode lineshapes are obtained only when the inhomogeneous broadening dominates the homogeneous broadening. A genuinely amplitude-modulated signal is obtained when the contributions of the shifted-echo and shifted-antiecho pathways are equal. However, as a consequence of the properties of whole echoes, a hypercomplex two-dimensional Fourier transform still gives rise to pure absorption-mode lineshapes even when the contributions of the two pathways are unequal. Sign discrimination must again be restored using the States–Haberkorn–Ruben or TPPI methods. An important further point to note is that it is necessary to use the much longer spin-echo interval required by the shifted-antiecho sequence.

CONVERSION OF TRIPLE- TO SINGLE-QUANTUM COHERENCE

An important part of all MQMAS experiments is the pulse which converts triple-quantum coherences into single-quantum coherences of the central transition. Consideration of the coherence transfer pathway diagrams in Fig. 1 shows that there are two different changes in coherence order, $|\Delta p|$, associated with this pulse, namely $|\Delta p| = 2$ and $|\Delta p| = 4$. It is, therefore, instructive to examine the flip-angle dependence of the efficiency of the two different conversions. Figures 5a–5c show such plots for different ratios of the quadrupolar frequency, ω_Q^{PAS}, to the inherent nutation frequency of the pulse, $\omega_1 = -\gamma B_1$.

From Fig. 5a, it is seen that, for a "hard" pulse, where $\omega_Q^{PAS}/\omega_1 \approx 0$, the two amplitudes are equal when the flip angle equals 90°, i.e., $\omega_1\tau_p = \pi/2$, where τ_p is the pulse duration; this is a familiar result from NMR of liquids (*43*). Furthermore, in this limit, the maximum transfer intensities for the $|\Delta p| = 2$ and $|\Delta p| = 4$ pathways are the same, although that for $|\Delta p| = 2$ occurs at a lower flip angle (70.5°) than that for $|\Delta p| = 4$ (109.5°). An obvious, though significant, point is that the maximum coherence transfer intensities for the individual pathways are greater than the transfer intensity corresponding to the flip angle where the two conversions are equal.

In MQMAS experiments, it is usually the case that, even using the most powerful amplifiers currently available, the
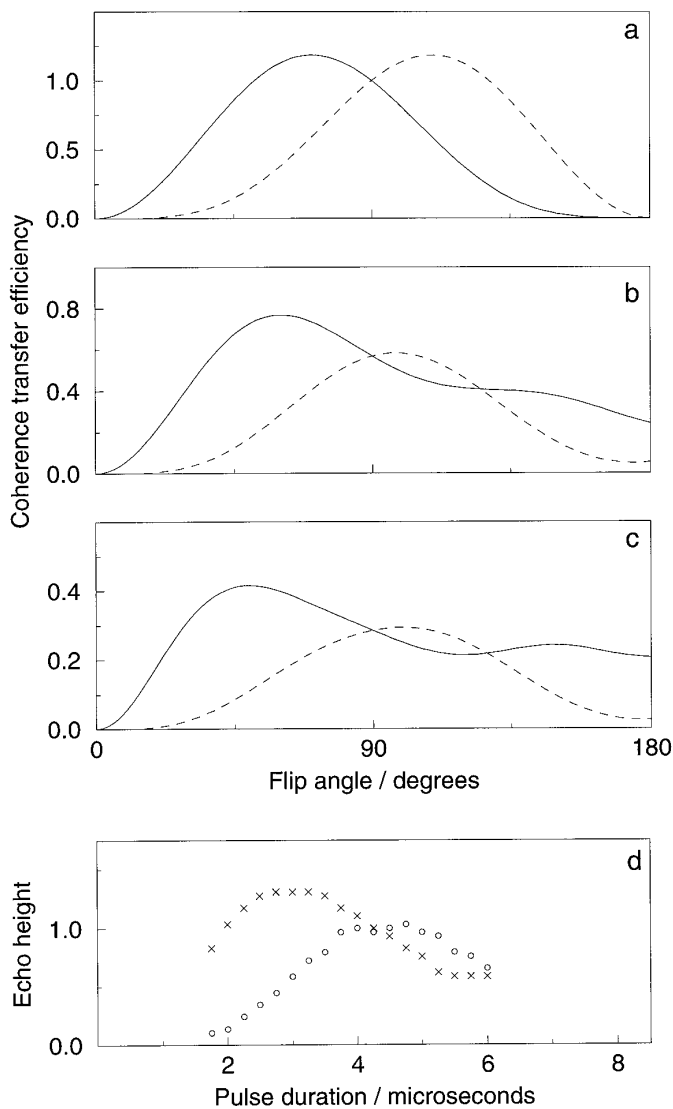
FIG. 5. (a–c) Calculated efficiency of coherence transfer between coherence orders $p = +3$ and $p = +1$ (solid line) and $p = -3$ and $p = +1$ (dashed line) for a spin $I = 3/2$ nucleus over a range of values of the inherent pulse flip angle $\omega_1\tau_p$. (These plots also represent the efficiency of coherence transfer between coherence orders $p = -3$ and $p = -1$ (solid line) and $p = +3$ and $p = -1$ (dashed line).) The single-quantum coherences ($p = \pm 1$) are those of the central transition only. The ratio $|\omega_Q^{PAS}/\omega_1|$ is 0.0 in (a), 2.5 in (b), and 5.0 in (c). The efficiency of coherence transfer has been normalized such that it is equal to 1.0 for the intense ($\omega_1 \gg \omega_Q^{PAS}$) 90° pulse in (a). The calculation assumes a powder distribution of crystallite orientations. (d) Experimental efficiency of coherence transfer between coherence orders $p = +3$ and $p = +1$ (crosses) and $p = -3$ and $p = +1$ (circles) over a range of pulse durations for ^{87}Rb NMR (98.2 MHz) of RbNO$_3$. The results were obtained by measuring the height of the echo for the shifted-antiecho and shifted-echo experiments in Fig. 1b, respectively. The vertical scale in (d) has been normalized such that it is equal to 1.0 where the two efficiencies are equal, corresponding to an inherent 90° pulse.

field strength, ω_1, is significantly less than ω_Q^{PAS}; this is the situation shown in Figs. 5b and 5c, where ω_Q^{PAS}/ω_1 equals 2.5 and 5, respectively. The following important features are

evident from these plots. First, the two pathways are again equal when the inherent flip angle equals 90° (*2, 12*). Second, the maximum transfer intensity is now greater for the smaller coherence transfer change, $|\Delta p| = 2$ (*25*), with this maximum occurring at a lower flip angle as before. It is also important to note that as ω_Q^{PAS}/ω_1 increases the magnitude of the transfer intensity decreases (*5*).

It is well known that, unless $\omega_Q/\omega_1 \approx 0$, the rate at which the central transition nutates during a pulse is not equal to the inherent nutation rate, ω_1 (*36, 37*). Experimentally, therefore, we have found that the easiest way to determine the inherent 90° flip angle is to compare, for a range of flip angles, the heights of the time-domain echo or the frequency-domain peak for the shifted-echo and shifted-antiecho experiments of Fig. 1b or the simple echo and simple antiecho experiments of Fig. 1a, respectively. Figure 5d presents ^{87}Rb experimental transfer intensities obtained, by measuring the signal in the shifted-echo and shifted-antiecho experiments, for a sample of RbNO$_3$. It is clear that the same features, as seen in the simulations, are observed. In particular, the $|\Delta p| = 2$ change is more efficient than the $|\Delta p| = 4$ change. (It should be noted that this plot is in fact a superposition of three curves, associated with the three crystallographically inequivalent Rb sites in the unit cell. There is, however, not much difference between the shapes of the individual curves, since the difference in ω_Q between the sites is small.) The results in Fig. 5d were obtained on a Bruker AC 300 spectrometer, equipped with only a 300 W radiofrequency amplifier, such that ω_Q^{PAS}/ω_1 ranged between 7.1 and 8.2 for the three sites (using the C_Q values given in Ref. (*4*)). Analogous ^{23}Na NMR results for Na$_2$SO$_4$ have recently been presented in Ref. (*12*).

It was stated earlier that pure absorption-mode lineshapes are obtained in the simple amplitude-modulated experiment when the two pathways are combined with equal amplitude. An important question to ask is, what happens when the flip angle of the triple- to single-quantum coherence conversion pulse is such that the two pathways are not combined with equal amplitude? Figures 3a and 3b showed the effect of a complex two-dimensional Fourier transform on simulated data sets resulting from the separate echo and antiecho pathways of Fig. 1a. When the two pathways add up with equal intensity in the simple amplitude-modulated experiment, the dispersive parts of the lineshapes cancel leaving a pure absorption-mode lineshape. This is demonstrated in Fig. 6a.

Figures 6b and 6c show what happens when different combinations of the spectra from the two pathways are added up. The ratios of the echo to antiecho pathways equal 0.7 and 2.5, respectively, and were chosen to correspond to those in the experimental spectra in Figs. 6e and 6f. From these contour plots, it is evident that the degree of dispersive character only becomes significant in Fig. 6c, where the ratio of the two pathways differs considerably from unity. Figures 6d–6f show experimental ^{87}Rb spectra of RbNO$_3$ obtained with the simple amplitude-modulated experiment in Fig. 1a,
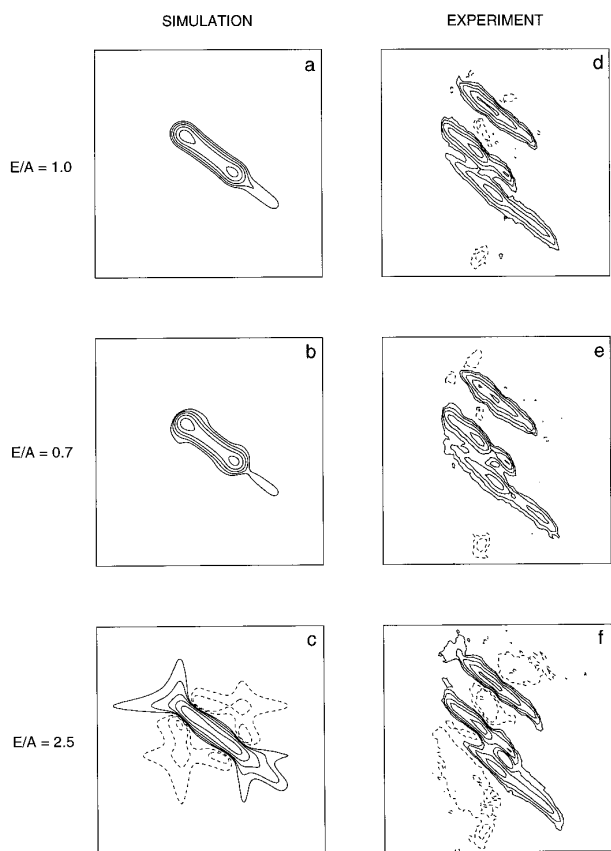
FIG. 6. Contour plots of simulated (a–c) and experimental (d–f) spectra obtained with the simple amplitude-modulated experiment in Fig. 1a, where the echo and antiecho pathways are combined with different amplitudes. The ratio of the two pathways is denoted E/A and is indicated in the figure. The contour plots in (d–f) show 6×6 kHz regions of ^{87}Rb NMR (98.2 MHz) spectra of RbNO$_3$. The full F_1 and F_2 spectral widths were 40 and 25 kHz, respectively; 192 transients (consisting of 512 points each) were averaged for each of 192 increments of t_1; and the relaxation interval was 100 ms. The duration of the triple-quantum excitation pulse was 8.5 μs. The duration of the $p = \pm 3$ to $p = -1$ reconversion pulse was 4.3, 5.3, and 2.8 μs in (d), (e), and (f), respectively.

where the flip angle of the $p = \pm 3$ to $p = -1$ conversion pulse is varied. The spectra were recorded at the same time as the results in Fig. 5d, and the ratio of the two pathways, $|\Delta p| = 2$ to $|\Delta p| = 4$, can be read off from Fig. 5d, namely (d) 1 at 4.25 μs, (e) 0.7 at 5.25 μs, and (f) 2.5 at 2.75 μs. As in the simulations, there is evidence of significant dispersive character only in (f), where the ratio differs most from unity.

As an alternative to having to calibrate carefully the flip angle of the conversion pulse, Amoureux *et al.* have recently presented an experiment where the $p = \pm 3$ coherences are converted to $p = -1$ coherences via a population state, $p = 0$ (*22*). The symmetry of such a z-filtered (*44*) experiment means that the two pathways always combine with equal amplitude.
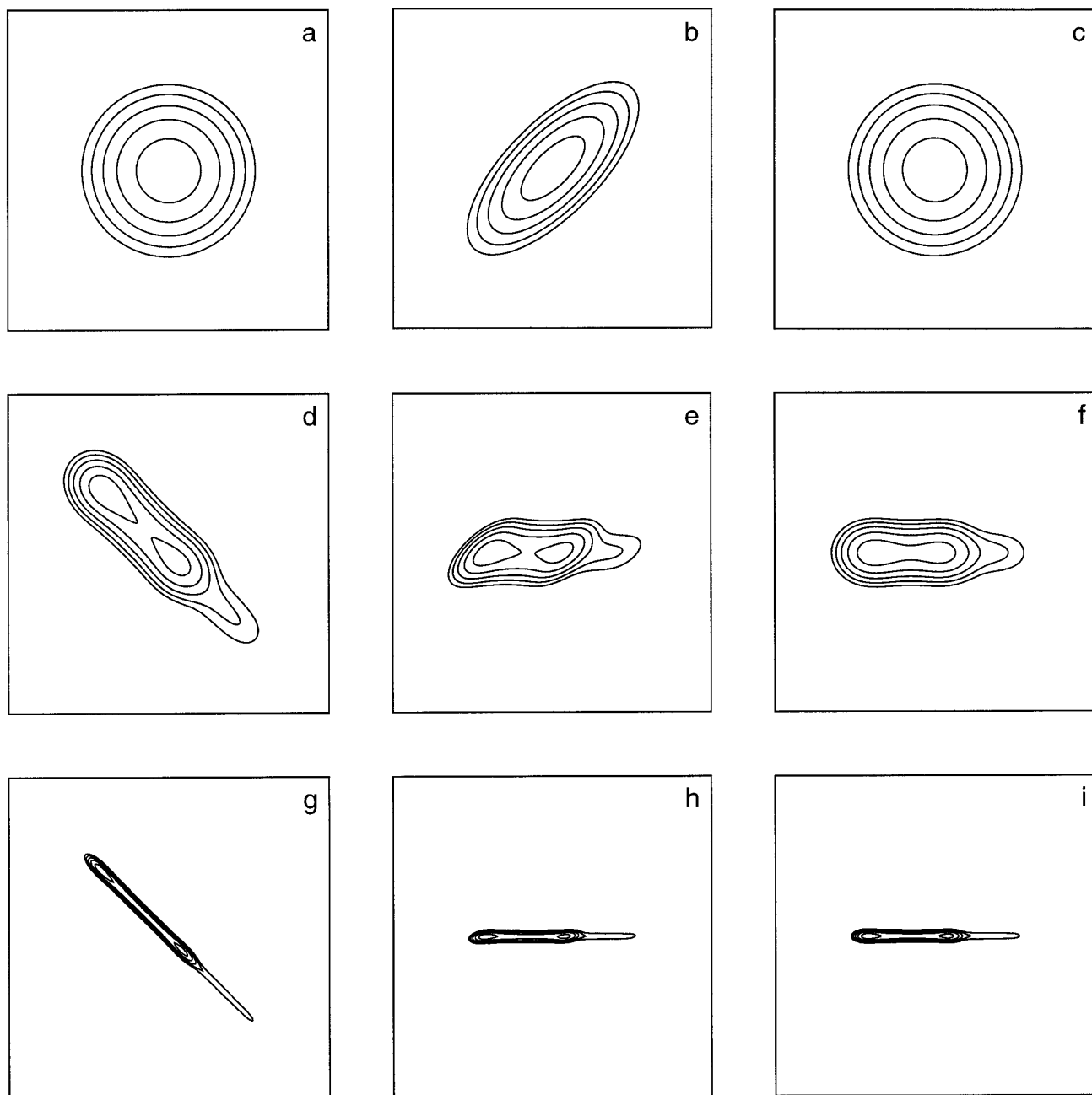
SHEARING

In the discussions so far, it has simply been stated that the inhomogeneous quadrupolar broadening is spread out

along a ridge, the gradient of which depends on the MQMAS ratio. The main purpose of performing these MQMAS experiments is to obtain a spectrum displaying only isotropic shifts (both chemical and second-order quadrupolar in origin). Such a spectrum corresponds to the projection of the two-dimensional spectrum onto an axis orthogonal to the ridges. In practice, such a projection is more easily obtained by, first, performing a shearing transformation such that the ridges appear parallel to the F_2 axis. To avoid interpolation problems, it is preferable to perform the shearing transformation in the mixed frequency–time domain, $S(t_1, \omega_2)$. Gradinetti *et al.* (*31*) have shown that this shearing transformation corresponds to the application of the following t_1-dependent first-order phase correction (*38*),

$$S'(t_1', \omega_2') = \exp\{-iG\omega_2 t_1\} S(t_1, \omega_2), \qquad [11]$$

where G denotes the gradient of the ridge in the frequency domain, which equals plus or minus the MQMAS ratio, depending on the sign of the triple-quantum coherence which evolves during t_1. It is important to note that $S(t_1, \omega_2)$ must be complex and, in particular, the phase correction cannot be used with amplitude-modulated data sets in which sign discrimination has not been restored. As discussed in Refs. (*4, 14*), shearing the data set reduces the spectral width in F_1 by a factor, using the notation of Table 1, of $|C_{1/2}^I|/(|C_{1/2}^I| + |C_{3/2}^I|)$, i.e., 9/16 for spin $I = 3/2$.

Shearing, however, is not a perfect solution, even if carried out in the $S(t_1, \omega_2)$ domain. Although it must be stressed that shearing does not affect the isotropic projection, it can cause distortions in the two-dimensional lineshapes. Figure 7 shows how the ratio of the inhomogeneous to homogeneous broadening affects the degree of distortion associated with shearing. The top row of Fig. 7 illustrates the case where there is no inhomogeneous broadening, and Fig. 7a is simply a plot of a two-dimensional pure absorption-mode Gaussian lineshape. Figures 7d and 7g correspond to a summation of Gaussian lineshapes along the diagonal $F_1 = -F_2$, such that the projection onto an axis parallel to the ridge is a typical second-order quadrupolar broadened spectrum. The ratio of the inhomogeneous to homogeneous broadening is greater in Fig. 7g, and the ridge is seen to be considerably narrower. Figures 7b, 7e, and 7h show the effect of performing a shearing transformation on the frequency-domain data sets of Figs. 7a, 7d, and 7g, respectively. For comparison, Figs. 7c, 7f, and 7i illustrate the case where the same Gaussian lineshapes add up parallel to the F_2 axis. It is clear that the degree of distortion associated with shearing decreases as the ratio of the inhomogeneous to homogeneous broadening increases. A frequency-domain shearing transformation was used in Figs. 7b, 7e, and 7h but, for the special case of a 1:1 ridge (i.e., one along $F_1 = \pm F_2$), there are no interpolation problems associated with this method. Exactly the same result would have been obtained if the shearing had been performed in the mixed frequency–time domain using Eq. [11].

FIG. 7. Contour plots showing how the ratio of the inhomogeneous to homogeneous broadening affects the degree of distortion associated with shearing. In (a–c), there is no inhomogeneous broadening, while in (d–f) and (g–i) significant inhomogeneous broadening is present, with the ratio taking its largest value in (g–i). In (d) and (g), two-dimensional Gaussian lineshapes are summed along the diagonal $F_1 = -F_2$, such that the projection onto an axis parallel to the ridge is a typical second-order quadrupolar broadened spectrum. The middle column (b, e, h) shows the effect of performing a shearing transformation on the lineshapes in (a, d, g). For comparison, the right-hand column (c, f, i) illustrates the case where the same Gaussian lineshapes are summed parallel to the F_2 axis.

The undesirable effects associated with shearing are further demonstrated by the experimental ^{23}Na NMR spectra in Fig. 8. Figure 8a shows an unsheared spectrum, displaying two of the three crystallographically inequivalent sites in Na_2HPO_4, obtained with the simple amplitude-modulated experiment in Fig. 1a. Two ridges are seen in the center of the spectrum with spinning sidebands

either side, the ratio of the inhomogeneous to homogeneous broadening being greater for the lower ridge. The spectrum in Fig. 8b corresponds to the same experimental data set as in Fig. 8a, except that, as described above, a shearing transformation has been performed in the $S(t_1, \omega_2)$ domain, such that the ridges now lie parallel to the F_2 axis. It is clear that the broader ridge, in particular, has
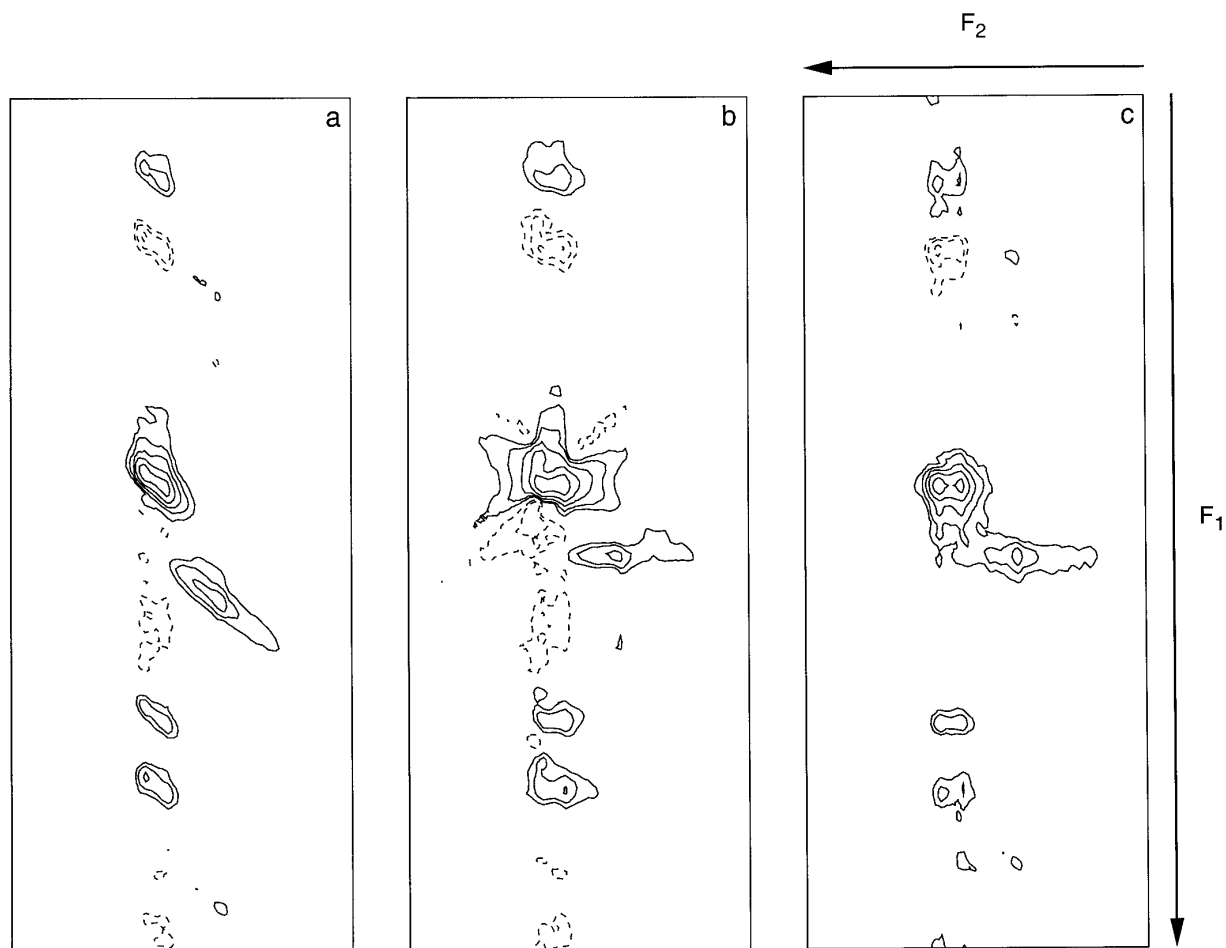
FIG. 8. Contour plots taken from ^{23}Na NMR (105.8 MHz) spectra of Na$_2$HPO$_4$ obtained with (a, b) the simple amplitude-modulated experiment in Fig. 1a and (c) the amplitude-modulated split-t_1 experiment in Fig. 9a. In (a), the displayed F_1 and F_2 spectral widths are 15 and 6 kHz, respectively. The spectrum in (b) is the result of applying a shearing transformation in the $S(t_1, \omega_2)$ domain, as described in the text, to the data set in (a). The shearing transformation reduces the F_1 spectral width by 9/16, such that the displayed F_1 spectral width is 8.4 kHz in (b). For comparison, the displayed F_1 and F_2 spectral widths in (c) are 8.4 and 6 kHz, respectively. It was not necessary to apply a shearing transformation in (c). Experimental conditions as similar as possible were used for the two experiments: the full F_2 spectral width was 25 kHz, 192 transients (consisting of 512 points each) were averaged for each of 128 increments of t_1, and the relaxation interval was 1 s. The duration of the triple-quantum excitation pulse was 8.0 μs. Sign discrimination was restored using the TPPI method of incrementing the phase of the first pulse by 30° for each increment of t_1. The full F_1 spectral width equaled 25 and 14.1 kHz in (a) and (c), respectively. The duration of the $p = \pm 3$ to $p = -1$ reconversion pulse in (a) was 3 μs, while that of the $p = +3$ to $p = +1$ and $p = -3$ to $p = -1$ conversion pulse in (c) was 1.5 μs. The first and second pulses in the z filter in (c) had duration 1 and 20 μs, respectively, with the radiofrequency field strength, $\omega_1/2\pi$, reduced to 6 kHz for the latter pulse.

been distorted by the shearing transformation (although this would not affect the isotropic projection). The spectrum in Fig. 8c corresponds to an experiment described in the following section, where undistorted ridge lineshapes appear parallel to the F_2 axis.

REFOCUSING THE ANISOTROPIC QUADRUPOLAR BROADENING IN t_1

The previous section showed that shearing can cause unwanted distortions in two-dimensional lineshapes. Although an undistorted spectrum showing isotropic shifts (the projection onto the F_1 axis after shearing) can still be obtained,

problems occur when F_2 cross sections through the two-dimensional spectrum are used to extract the parameters C_Q and η, especially when lineshapes overlap. This section describes modified amplitude- and phase-modulated experiments where the ridges appear parallel to the F_2 axis without the need for a shearing transformation. As shown in Figs. 7c, 7f, and 7i, this yields two-dimensional lineshapes that are completely free of distortion.

The key feature of all MQMAS experiments is the refocusing of the $l = 4$ anisotropic broadening when the ratio of the durations of the single- and triple-quantum evolution periods equals the magnitude of the MQMAS ratio. In all of the experiments introduced so far, this refocusing has
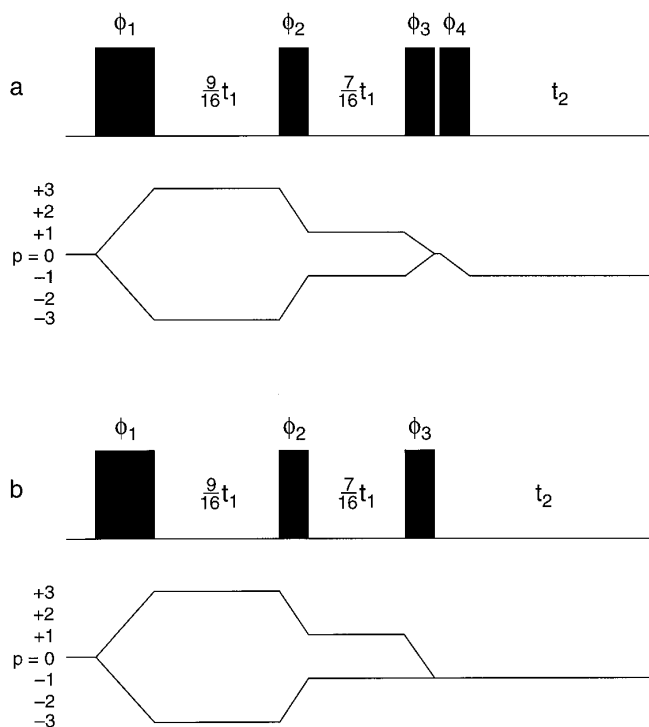
FIG. 9. Pulse sequences and coherence transfer pathway diagrams for two amplitude-modulated split-t_1 experiments (for spin $I = 3/2$ nuclei). The experiment in (a) uses a z filter at the end of the evolution period, t_1, while that in (b) uses a single pulse to transfer the two mirror-image pathways into observable coherence. The evolution period is split between single- and triple-quantum evolution according to the MQMAS ratio as indicated. The optimum flip angles for the individual pulses are described in the text. The interval between the third and fourth pulses in (a) is of negligible duration (~ 3 μs). Phase cycling schemes for the pulse phases ϕ_1, ϕ_2, ϕ_3, and ϕ_4 and for the receiver R_x are given in Table A3 of the Appendix.

occurred within the t_2 period. If, however, the t_1 period is split into single- and triple-quantum evolution periods in the ratio of the MQMAS ratio, the $l = 4$ anisotropic broadening is refocused at the end of the t_1 period, for all values of t_1 (10, 25). This refocusing of the quadrupolar broadening at $t_2 = 0$ means that undistorted inhomogeneously broadened ridges appear parallel to the F_2 axis without the need for a shearing transformation. Furthermore, as discussed later, the fact that the signal always appears at the same position in t_2 has important advantages, in particular with regard to achieving the optimum sensitivity.

Amplitude-Modulated Split-t_1 Experiments

Figure 9 shows the pulse sequence and coherence transfer pathway diagrams for amplitude-modulated experiments where the t_1 period can be seen to be split into single- and triple-quantum evolution periods in the ratio of the MQMAS ratio (10). As with the simple amplitude-modulated experiment, sign discrimination in F_1 can again be restored by using the States–Haberkorn–Ruben or TPPI methods.

To obtain genuinely pure absorption-mode lineshapes, it is necessary that the two mirror-image coherence transfer pathways combine with equal amplitude. This can be achieved most reliably, for all pulse powers, using a z filter (44), as shown in Fig. 9a. The flip angles of the two pulses of the z filter should be set equal to 45° pulses (i.e., for optimum sensitivity, they should be fully selective ($\omega_1 \ll \omega_Q$) 90° pulses on the central transition). Figure 8c presents an experimental ^{23}Na spectrum of Na$_2$HPO$_4$ for this experiment. It can be seen that, unlike in Fig. 8b, undistorted ridges, lying parallel to the F_2 axis, are obtained. It should be noted that the data sets leading to the spectra in Fig. 8 were recorded using experimental conditions that were as similar as possible. In particular, although the full spectral width in F_1 equals 25 and 14.0625 kHz, respectively, for Figs. 8a and 8c, shearing reduces the spectral width by $9/16$ and, therefore, the F_1 spectral widths are the same in Figs. 8b and 8c. This is unsurprising since the triple-quantum evolution period is incremented by the same amount and the echo forms at the same time in both experiments.

The z-filtered split-t_1 experiment in Fig. 9a requires two pulses more than the simple amplitude-modulated experiment in Fig. 1a and, if these pulses cannot be fully optimized, this will result in reduced sensitivity. An alternative is to use a single pulse to convert between $p = \pm 1$ and $p = -1$ coherences, as shown in Fig. 9b. It was stated earlier, for the simple amplitude-modulated experiment in Fig. 1a, that the coefficients of the $p = +3$ to $p = -1$ and $p = -3$ to $p = -1$ coherence transfer steps are the same, for all values of ω_Q^{PAS}/ω_1, if a 90° pulse is used. This is illustrated again in Fig. 10a, this time for a single value of the quadrupolar splitting parameter ω_Q, where the curves showing the transfer efficiencies of the $|\Delta p| = 2$ and $|\Delta p| = 4$ steps as a function of ω_Q/ω_1 are fully coincident for a 90° pulse. Unfortunately, for the split-t_1 experiment in Fig. 9b, there is no single flip angle where the coefficients of the $p = +1$ to $p = -1$ and $p = -1$ to $p = -1$ coherence transfer steps are the same for all values of ω_Q/ω_1. However, as shown in Fig. 10b, when the inherent flip angle is 45° the difference between the two transfer coefficients is small. Note that, as the magnitude of ω_Q/ω_1 increases, the two curves converge and that the efficiency of coherence transfer increases. Clearly, the optimum pulse for this coherence transfer step, therefore, is a 45° pulse with $\omega_1 \ll \omega_Q$, i.e., a fully selective 90° pulse on the central transition.

Figure 11 presents ^{23}Na NMR spectra of a mixture of Na$_2$SO$_4$ and Na$_2$C$_2$O$_4$ obtained with the simple amplitude-modulated experiment in Fig. 1a and the amplitude-modulated split-t_1 experiment in Fig. 9b. Experimental conditions as similar as possible were again used, although, as discussed above, the duration of the pulse which combines the two pathways equaled 3.7 and 1.9 μs (equivalent to inherent 90° and 45° flip angles) in Fig. 11a and Fig. 11c, respectively. As predicted in Fig. 7, it is clear from Fig. 11b that, with long narrow ridges, shearing does not produce any distortion
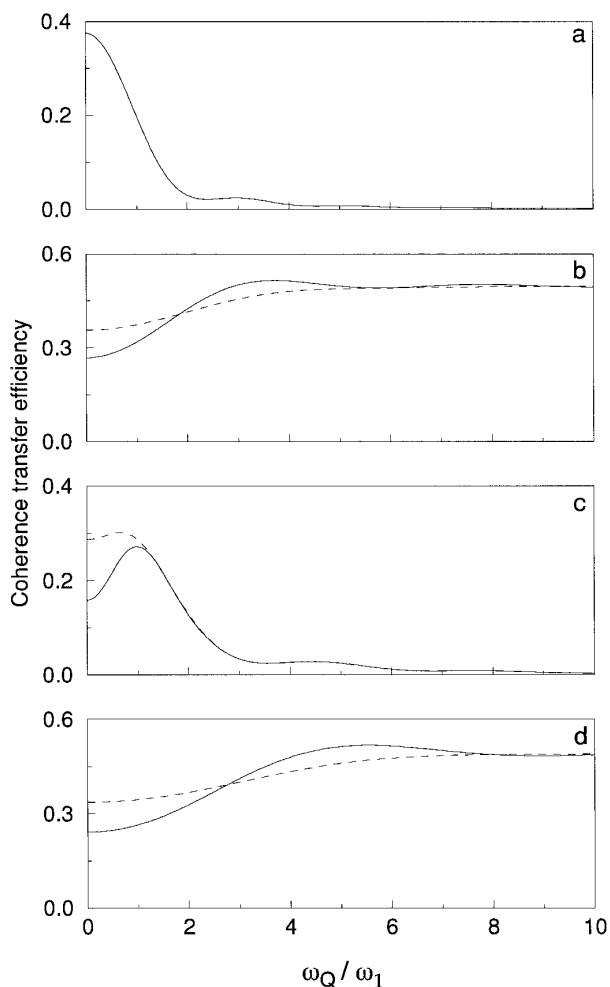
FIG. 10. Plots comparing the efficiency of coherence transfer as a function of $|\omega_Q/\omega_1|$ between coherence orders $p = -3$ and $p = -1$ (solid line) and $p = +3$ and $p = -1$ (dashed line) in (a) and (c) and $p = -1$ and $p = -1$ (solid line) and $p = +1$ and $p = -1$ (dashed line) in (b) and (d). The single-quantum coherences ($p = \pm 1$) are those of the central transition only. It should be noted that the two curves are superimposed in (a). The plots in (a) and (b) are for spin $I = 3/2$ nuclei, while those in (c) and (d) are for spin $I = 5/2$ nuclei. In each case, the optimized flip angle is used such that the difference between the two transitions is minimized. The inherent flip angle $\omega_1 \tau_p$ equals 90° in (a), 45° in (b), 60° in (c), and 30° in (d). The vertical scale gives the normalized coherence transfer amplitudes calculated for the relevant states expressed in a single-element operator basis.

of the lineshape. Using the pulse sequence in Fig. 9b, pure absorption-mode lineshapes are apparently obtained in Fig. 11c although, in order to achieve this, full radiofrequency power had to be used for the final pulse. This is a good example of what we have found generally in our work with amplitude-modulated MQMAS experiments: that it is straightforward to achieve pure absorption-mode lineshapes in z-filtered experiments, but much more difficult to achieve them in single-pulse conversion experiments. Finally, it is interesting to note that in all parts of both Fig. 8 and Fig. 11 spinning sidebands appear at 7/16 and 9/16 of the spin-

ning speed, corresponding to single- and triple-quantum evolution, respectively.
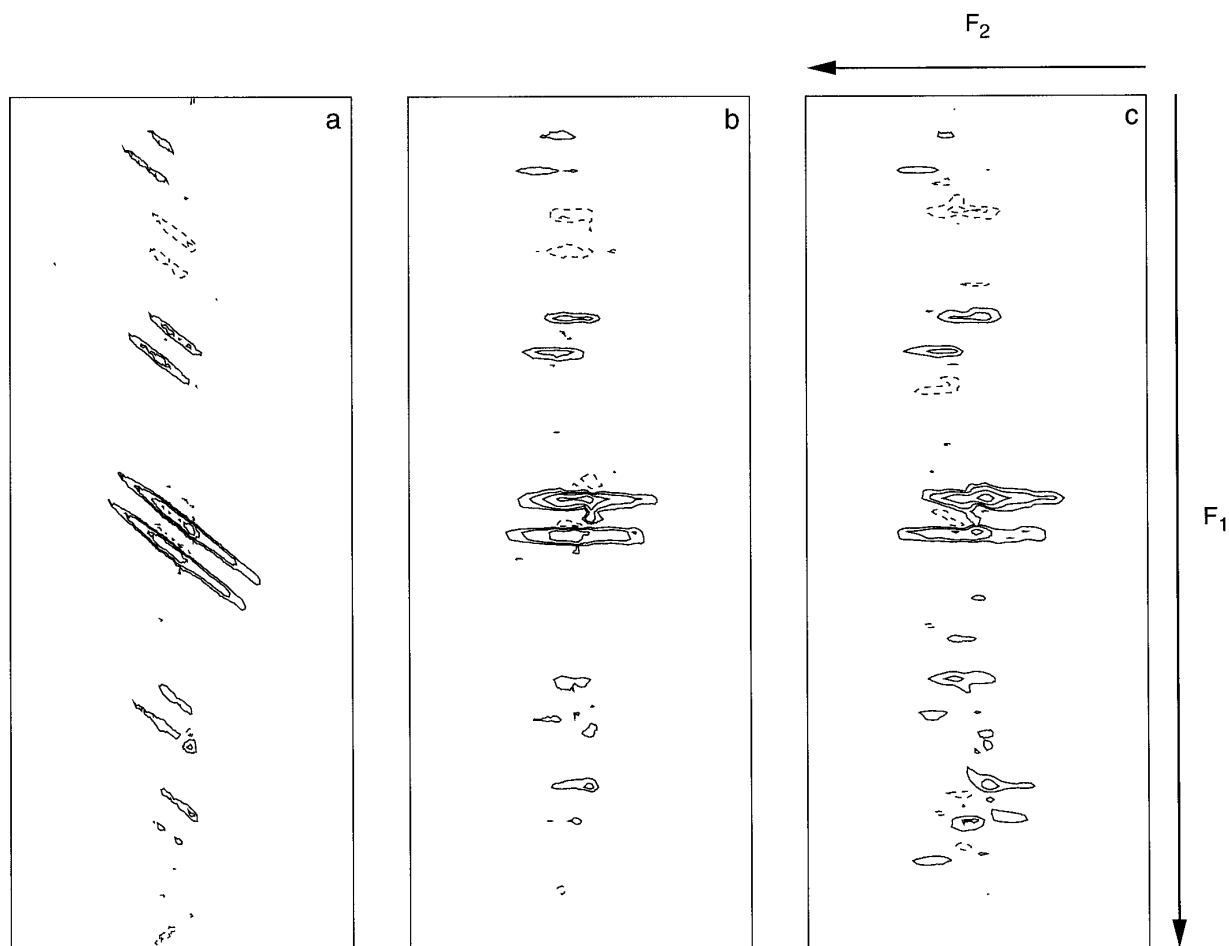
Phase-Modulated Split-t_1 Experiments

We have also recently presented phase-modulated split-t_1 experiments (25), which are shown in Fig. 12. It can be seen that two alternative pathways can be selected, which differ in the change of coherence order induced by the second pulse. It was shown earlier that the maximum coherence transfer efficiency for $|\Delta p| = 2$ is greater than that for $|\Delta p| = 4$, and hence the sequence in Fig. 12a is to be preferred. The experiments in Fig. 12 involve the correlation of triple- and single-quantum coherences of the same sign, and are, therefore, modified versions of the shifted-echo sequence. (Similarly modified versions of the shifted-antiecho sequence also exist; however, as discussed earlier, a much longer spin-echo interval is necessary in this case.)

Comparison of the shifted-echo experiment in Fig. 1b and the split-t_1 experiment in Fig. 12b reveals that they differ only in how t_1 is defined, and hence there is no inherent difference in resolution or sensitivity between the two approaches. Furthermore, it was shown earlier that phase-modulated whole-echo experiments give rise to pure absorption-mode lineshapes only when the inhomogeneous broadening dominates the homogeneous broadening. In this limit, shearing does not distort the two-dimensional lineshape. However, it is shown in the next section that there are still important advantages associated with using the split-t_1 experiments.

Figure 13 presents ^{87}Rb NMR spectra of $RbNO_3$ obtained with the phase-modulated shifted-antiecho experiment in Fig. 1b and the phase-modulated split-t_1 experiment in Fig. 12a. The triple- to single-quantum conversion pulses were calibrated to optimize the amplitude of the $|\Delta p| = 2$ coherence transfer step and had the same duration in both the shifted-antiecho (Fig. 13a) and the split-t_1 experiment (Fig. 13c). For further comparison, the spectrum of $RbNO_3$ was also recorded using the shifted-echo experiment in Fig. 1b with the flip angle of the conversion pulse optimized for the $|\Delta p| = 4$ coherence transfer step (not shown). The signal-to-noise ratios obtained with these three comparable experiments are discussed in the next section. Note that there is no evidence of any distortion of the two-dimensional lineshapes in the sheared spectrum in Fig. 13b.

SIGNAL-TO-NOISE CONSIDERATIONS

With so many experiments to choose from, a vital question to ask is, which experiment yields the best signal-to-noise ratio (henceforth denoted S/N)? Schematic representations of time-domain data sets for the simple amplitude-modulated experiment, the shifted-echo experiment, and the amplitude-modulated whole-echo experiment are given in Figs. 2e, 2c, and 2f, respectively. Initially, an idealized situation will be

F$_2$

F$_1$

FIG. 11. Contour plots taken from ^{23}Na NMR (105.8 MHz) spectra of a mixture of Na$_2$C$_2$O$_4$ and Na$_2$SO$_4$ obtained with (a, b) the simple amplitude-modulated experiment in Fig. 1a and (c) the amplitude-modulated split-t_1 experiment in Fig. 9b. In (a), the displayed F_1 and F_2 spectral widths are 25 and 10 kHz, respectively. The spectrum in (b) is the result of applying a shearing transformation in the $S(t_1, \omega_2)$ domain, as described in the text, to the data set in (a). The shearing transformation reduces the F_1 spectral width by 9/16, such that the displayed F_1 spectral width is 14.1 kHz in (b). For comparison, the displayed F_1 and F_2 spectral widths in (c) are 14.1 and 10 kHz, respectively. It was not necessary to apply a shearing transformation in (c). Experimental conditions as similar as possible were used for the two experiments: the full F_2 spectral width was 25 kHz, 96 transients (consisting of 256 points each) were averaged for each of 256 increments of t_1, and the relaxation interval was 1 s. The duration of the triple-quantum excitation pulse was 7.4 μs. Sign discrimination was restored using the TPPI method of incrementing the phase of the first pulse by 30° for each increment of t_1. The full F_1 spectral width equaled 50 and 28.1 kHz in (a) and (c), respectively. The duration of the $p = \pm 3$ to $p = -1$ reconversion pulse in (a) was 3.7 μs, while that of the $p = +3$ to $p = +1$ and $p = -3$ to $p = -1$ conversion pulse in (c) was 2.0 μs. The $p = \pm 1$ to $p = -1$ conversion pulse in (c) had duration 1.9 μs. The bottom contour in each spectrum corresponds to 8% of the maximum height.

considered where, first, there is no signal loss associated with the spin echo, and, second, the contributions of the echo and antiecho pathways are equal and the same in each of the experiments. When these simplifications are made, comparing the S/N of the three different experiments is relatively straightforward.

Examining first the amplitude-modulated whole-echo data set in Fig. 2f, it is evident that the time-domain signal is symmetric about the center of t_2, with each mirror image being identical to that of the simple amplitude-modulated data set in Fig. 2e. Therefore, the signal in Fig. 2f is double that in Fig. 2e. However, the noise is $\sqrt{2}$ greater, since the acquisition time in Fig. 2f is double that in Fig. 2e, and,

hence, there is only a $\sqrt{2}$ improvement in S/N between the two experiments.

Furthermore, when the contribution of the two pathways in the amplitude-modulated whole-echo experiment is equal, the imaginary part, after performing the Fourier transform in the t_2 dimension, contains only noise, and can therefore be deleted and zero-filled. In contrast, in the phase-modulated whole-echo experiment, the imaginary part contains signal and cannot be deleted. There is, therefore, $\sqrt{2}$ less noise in the frequency domain for the amplitude-modulated whole-echo experiment. There is no difference in the height of the individual peaks, and, thus, the amplitude-modulated whole-echo experiment offers a $\sqrt{2}$ improvement in S/N over the
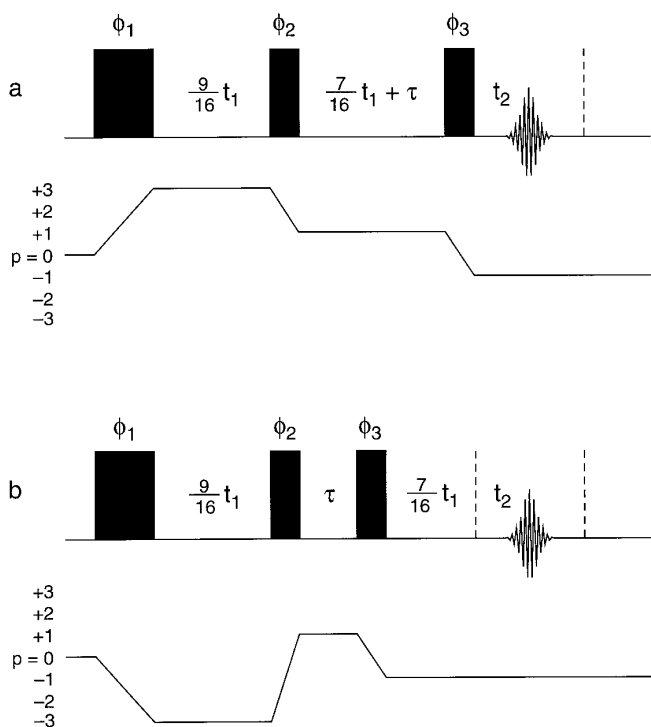
FIG. 12. Pulse sequences and coherence transfer pathway diagrams for two phase-modulated split-t_1 experiments (for spin $I = 3/2$ nuclei). The evolution period, t_1, is split between single- and triple-quantum evolution according to the MQMAS ratio as indicated. The second pulse changes the coherence order by $\Delta p = -2$ in (a) and by $\Delta p = +4$ in (b). As a result, if $\omega_1 < \omega_Q^{PAS}$, the sensitivity of the experiment in (a) is higher than that in (b) and makes it the phase-modulated experiment of choice for spin $I = 3/2$ nuclei. A whole echo always forms at the center of the acquisition period, t_2, for all values of t_1. The optimum flip angles for the individual pulses are described in the text. The spin-echo interval, τ, should be of sufficient length to ensure that the whole echo is not truncated. The phase cycling schemes for the pulse phases ϕ_1, ϕ_2, and ϕ_3 and for the receiver R_x are the same as those for the shifted-antiecho and shifted-echo experiments in Fig. 1b and are given in Table A2 of the Appendix.

phase-modulated whole-echo experiment. Thus, for these idealized data sets, the relative S/N of the three experiments is in the ratio of $1:1:\sqrt{2}$ for the simple amplitude-modulated, the phase-modulated whole-echo, and the amplitude-modulated whole-echo experiments, respectively.

Unsurprisingly, in practice, the situation is significantly more complicated than that discussed above for an idealized case. First, there will, of course, be signal loss associated with the spin echo as a consequence of transverse relaxation. Furthermore, if the pulse which inverts the central transition is not perfectly selective, additional signal will be lost. Clearly, these features will tend to degrade the S/N of the two whole-echo experiments in Fig. 1b relative to the simple amplitude-modulated experiment in Fig. 1a. In addition, to record the shifted-antiecho signal in the amplitude-modulated whole-echo experiment, it is necessary to use a much longer spin-echo interval than in the phase-modulated experiment. More signal is, hence, lost through relaxation, and

the $\sqrt{2}$ difference in S/N between the two experiments is significantly reduced.

A second important consideration is the relative contribution of the echo and antiecho pathways. For the idealized data sets discussed above, the contribution of the two pathways was assumed to be equal and the same in all data sets. However, Fig. 5 showed that the maximum coherence transfer amplitudes for the individual $|\Delta p| = 2$ or $|\Delta p| = 4$ steps are greater than the transfer amplitude when the two steps are equal. This has the consequence that the optimum flip angle for the triple- to single-quantum coherence conversion pulse differs between the three experiments and, hence, the S/N of the single-pathway, phase-modulated whole-echo experiment improves relative to the other two.

From the representations of the time-domain data sets in Fig. 2, it is evident that significant amounts of the acquisition time are spent recording only noise. In order to achieve optimum sensitivity, the application of time-domain filters, whose position changes as a function of t_1, has been proposed (4, 31). In both the simple amplitude-modulated and the amplitude-modulated whole-echo experiments, the proportion of the acquisition time occupied by signal increases as t_1 increases. For example, in Fig. 2e, at $t_1 = 0$, a half-echo forms in t_2, while at larger t_1, a whole echo forms. In contrast, in the phase-modulated whole-echo experiments, a whole echo of the same length is formed for all values of t_1. The consequence of this is that a greater amount of noise can be filtered out in the phase-modulated whole-echo experiments, hence increasing their S/N relative to that of the other two experiments.

This section has so far not discussed the split-t_1 experiments introduced in the previous section. Considering first the phase-modulated split-t_1 experiments in Fig. 12, it was stated in the previous section that there is no inherent difference in resolution or sensitivity between the experiment in Fig. 12b and the phase-modulated shifted-echo experiment of Fig. 1b. However, the processing required to obtain the optimum S/N is considerably simpler in the split-t_1 experiments. In addition to not needing to apply a shearing transformation, the key advantage is the fact that the echo always forms at the same position in t_2. This has the following favorable consequences. First, since the echo does not move through t_2, the length of the acquisition period, and hence the introduction of noise, can be kept to a minimum. There is, thus, no requirement to use t_1-dependent weighting functions to optimize the S/N. Second, to record an echo which is symmetric about its center, it is obvious that the center of the echo should correspond to the center of t_2. As discussed earlier, this means that it is very easy to apply the necessary phase correction to ensure that the center of the echo corresponds to $t_2 = 0$, when $t_1 = 0$.

Furthermore, there is an additional advantage of the phase-modulated split-t_1 experiment in Fig. 12a as a consequence of the $|\Delta p| = 2$ change being more efficient than the $|\Delta p|$
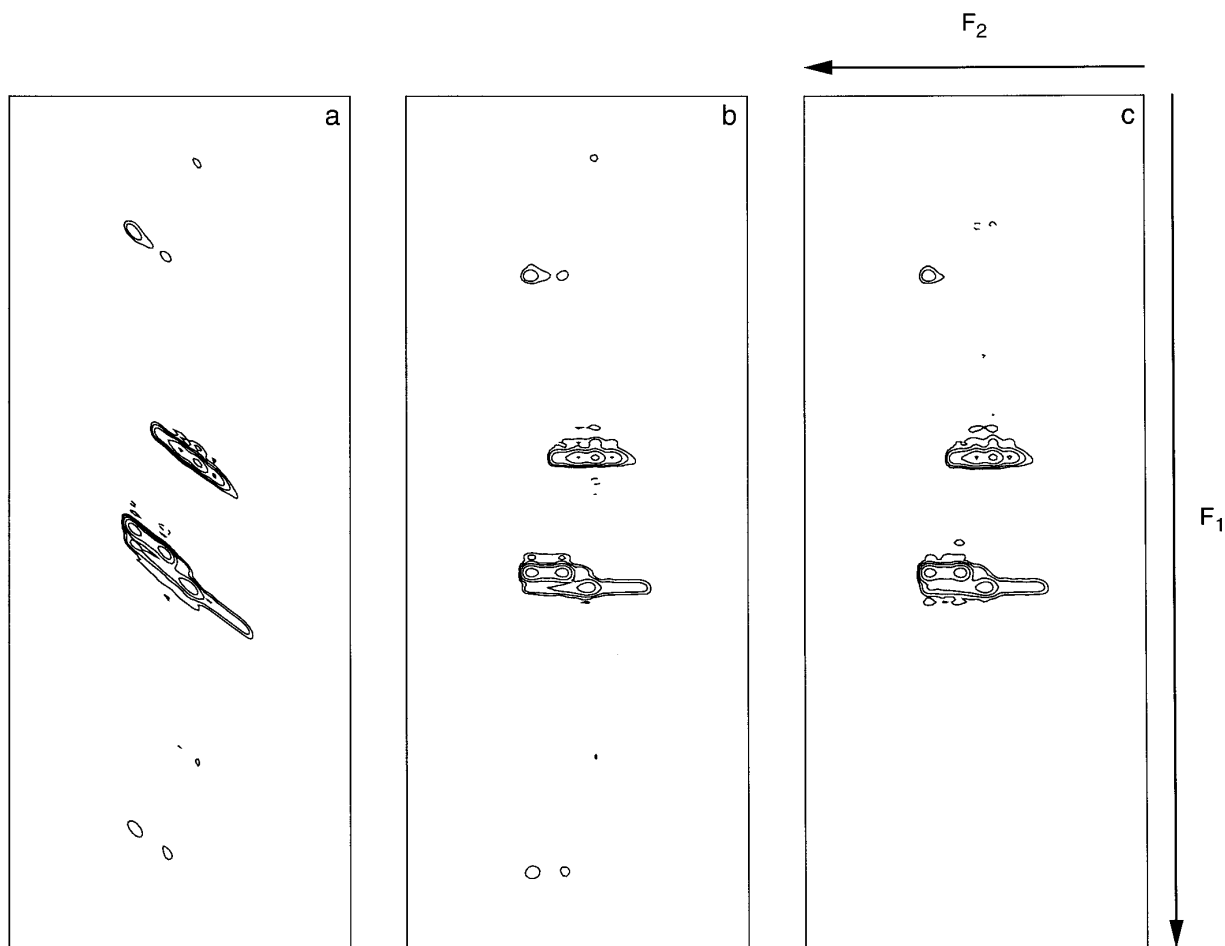
FIG. 13. Contour plots taken from ^{87}Rb NMR (130.9 MHz) spectra of RbNO$_3$ obtained with (a, b) the shifted-antiecho experiment in Fig. 1b (dashed line) and (c) the phase-modulated split-t_1 experiment in Fig. 12a. In (a), the displayed F_1 and F_2 spectral widths are 15 and 6 kHz, respectively. The spectrum in (b) is the result of applying a shearing transformation in the $S(t_1, \omega_2)$ domain, as described in the text, to the data set in (a). The shearing transformation reduces the F_1 spectral width by 9/16, such that the displayed F_1 spectral width is 8.4 kHz in (b). For comparison, the displayed F_1 and F_2 spectral widths in (c) are 8.4 and 6 kHz, respectively. It was not necessary to apply a shearing transformation in (c). Experimental conditions as similar as possible were used for the two experiments: the full F_2 spectral width was 29.4 kHz, 96 transients (consisting of 1024 and 512 points each in (a) and (c), respectively) were averaged for each of 192 increments of t_1, and the relaxation interval was 100 ms. The full F_1 spectral width equaled 44.4 and 25 kHz in (a) and (c), respectively. The durations of the triple-quantum excitation and the $p = +3$ to $p = +1$ conversion pulses were 6.8 and 1.0 μs, respectively. The duration of the central transition inversion pulse was 70 μs, with the radiofrequency field strength, $\omega_1/2\pi$, reduced to 4 kHz. The spin-echo interval, τ, was 7.8 ms in (a) and 4.4 ms in (c).

= 4 change. For the experiments in Fig. 1b, where there is only triple-quantum coherence evolution during t_1, it is the shifted-antiecho sequence that has the favorable coherence order change. However, it was stated earlier that there will be greater signal loss due to relaxation in the shifted-antiecho sequence as a consequence of the longer spin-echo interval. In contrast, the split-t_1 experiment in Fig. 12a has both the optimum coherence order change and the optimum spin-echo interval. These results are confirmed by measurements of S/N from the ^{87}Rb NMR spectra in Fig. 13 and from the ^{87}Rb spectrum (not shown) obtained with the shifted-echo experiment recorded at the same time under identical conditions. The S/N obtained with the phase-modulated shifted-antiecho experiment was 1.6 times higher than that obtained

with the shifted-echo experiment, while that obtained with the phase-modulated split-t_1 experiment in Fig. 12a was 2.0 times higher. Hence, the predicted sensitivity advantage for spin $I = 3/2$ nuclei of the split-t_1 experiment in Fig. 12a is confirmed.

Turning to the amplitude-modulated split-t_1 experiments in Fig. 9, it is clear that at least one additional pulse is required relative to the simple amplitude-modulated experiment in Fig. 1a (as also for the z-filtered experiment recently proposed by Amoureux *et al.* (*22*)). Although the favorable $|\Delta p| = 2$ coherence transfer step is carried out by the triple- to single-quantum conversion pulse, it would still be expected that the amplitude-modulated split-t_1 experiments have poorer S/N. This was indeed

found to be the case in the experimental ^{23}Na NMR spectra in Fig. 8, where, recorded under as similar conditions as possible, the S/N in Fig. 8a was 1.5 times higher than that in the spectrum in Fig. 8c which was recorded with the z-filtered split-t_1 experiment in Fig. 9a. Nevertheless, depending on the particular experimental application, this modest reduction in sensitivity might be a price worth paying to ensure that undistorted lineshapes are obtained. The z-filtered experiment proposed by Amoureux *et al.* (*22*) yielded an even smaller sensitivity advantage over the z-filtered split-t_1 experiment: a ^{23}Na NMR spectrum of Na$_2$HPO$_4$ (not shown) recorded under comparable conditions to those used in Fig. 8c had a S/N that was only 1.1 times better. A numerical comparison, using our simulation programs, of the sensitivity of these three amplitude-modulated experiments yields excellent agreement with the experimental results. Note that, as with the phase-modulated split-t_1 experiments, the amplitude-modulated split-t_1 experiments in Fig. 9 have the practical advantage that the time-domain signal does not move within the acquisition period t_2, meaning that this can be kept short and that normal (i.e., t_1-independent) weighting functions can be used to optimize the S/N. It is also interesting to note that the S/N of the experiments in Fig. 9 can, in principle, be increased by a factor of $\sqrt{2}$ by appending a spin echo to the pulse sequence and acquiring a whole, rather than half, echo.

SPIN $I = 5/2$ NUCLEI

It was stated earlier that the MQMAS ratio for spin $I = 5/2$ equals $19/12$. The difference in sign to that for spin $I = 3/2$ (MQMAS ratio equals $-7/9$) means that the echo pathway now corresponds to the correlation of triple- and single-quantum coherences of opposite sign. The solid and dashed lines in Fig. 1 therefore now correspond to the anti-echo and echo pathways, respectively. The echo now forms at $t_2 = (19/12)t_1$, and the gradient of the inhomogeneously broadened ridge equals $19/12$.

For spin $I = 3/2$, the coherence transfer amplitudes for the $p = +3$ to $p = -1$ and the $p = -3$ to $p = -1$ steps are the same, for all values of ω_Q/ω_1, if a pulse with an inherent flip angle of 90° is used. For spin $I = 5/2$, there is no flip angle where the $p = \pm3$ to $p = -1$ amplitudes are the same for all values of ω_Q/ω_1. However, as shown in Fig. 10c, it is found that when a 60° pulse is used the difference between the two transitions is small. When this flip angle is used in the simple amplitude-modulated experiment, in most cases, apparently pure absorption-mode lineshapes are observed. To obtain genuinely pure absorption-mode lineshapes, it is necessary, as proposed by Amoureux *et al.,* to use a z-filtered sequence (*22*).

In split-t_1 MQMAS experiments for spin $I = 5/2$, the evolution time is now partitioned between single- and triple-quantum evolution in the ratio of $19/12$. As shown in
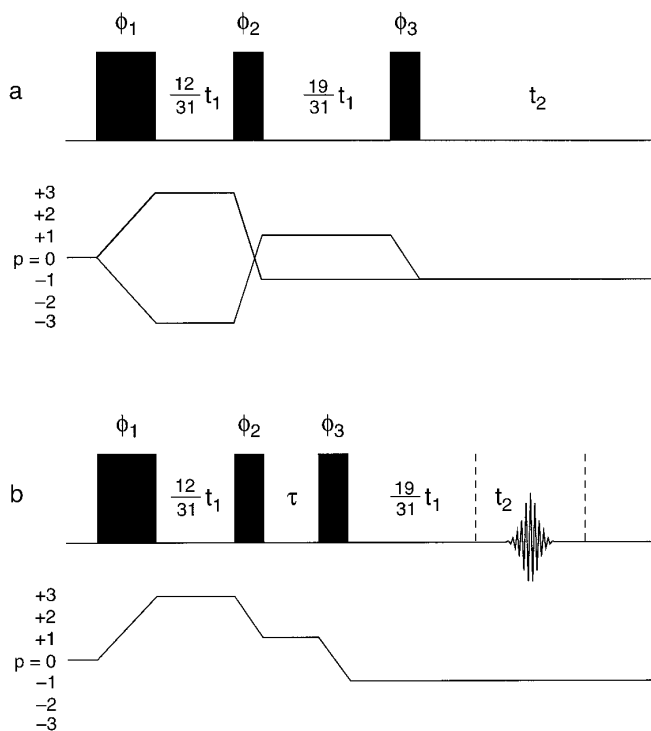
FIG. 14. The pulse sequence and coherence transfer pathway diagram for (a) an amplitude-modulated split-t_1 experiment and (b) the optimum phase-modulated split-t_1 experiment for spin $I = 5/2$ nuclei. The evolution period, t_1, is split between single- and triple-quantum evolution according to the MQMAS ratio as indicated. A whole echo always forms at the center of the acquisition period, t_2, for all values of t_1 in (b). The phase cycling scheme for the pulse phases ϕ_1, ϕ_2, and ϕ_3 and for the receiver R_x in (a) is given in Table A3 of the Appendix, while that in (b) is the same as that for the shifted-antiecho experiment in Fig. 1b and is given in Table A2 of the Appendix.

the pulse sequence and coherence transfer pathway diagram in Fig. 14a, the amplitude-modulated split-t_1 experiments involve the less favorable $|\Delta p| = 4$ triple- to single-quantum conversion step, although, as this is the only pathway selected, the conversion pulse flip angle can be optimized appropriately. For coherence transfer between $p = \pm1$ and $p = -1$ coherences at the end of the t_1 period, there is again no single flip angle where the two transfer amplitudes are the same for all values of ω_Q/ω_1. Figure 10d compares the two transfers for the optimum flip angle of 30°. Again it should be noted that, as the magnitude of ω_Q/ω_1 increases, the two curves converge and that the efficiency of coherence transfer increases. The optimum pulse for this coherence transfer step, therefore, is an inherent 30° pulse with $\omega_1 \ll \omega_Q$, i.e., a fully selective 90° pulse on the central transition. Alternatively, a z filter can be used, as with spin $I = 3/2$.

Figure 14b shows the pulse sequence and coherence transfer pathway diagram for a phase-modulated split-t_1 experiment which is optimized for spin $I = 5/2$. The experiment makes use of the more efficient $|\Delta p| = 2$ triple- to single-
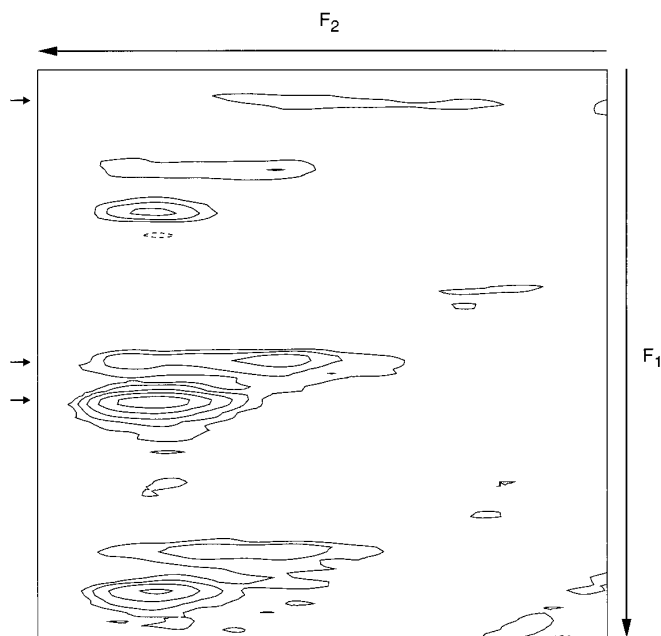
FIG. 15. A contour plot taken from a ^{27}Al NMR (104.2 MHz) spectrum of kyanite recorded using the phase-modulated split-t_1 experiment in Fig. 14b. The displayed spectral width is 10 kHz in both the F_1 and F_2 dimensions. The full F_1 and F_2 spectral widths were 38.7 and 50 kHz, respectively; 672 transients (consisting of 256 points each) were averaged for each of 192 increments of t_1; and the relaxation interval was 500 ms. The durations of the triple-quantum excitation and the $p = +3$ to $p = +1$ conversion pulses were 3.6 and 0.8 μs, respectively. The duration of the central transition inversion pulse was 30 μs, with the radiofrequency field strength, $\omega_1/2\pi$, reduced to 8 kHz. The spin-echo interval, τ, was 1.4 ms. It was not necessary to apply a shearing transformation. The isotropic shifts of the three identifiable ridges are marked with arrows in the F_1 dimension.

quantum conversion which means that, unlike in the optimum spin $I = 3/2$ experiment in Fig. 12a, the second part of the t_1 period now follows the final pulse. Figure 15 presents a ^{27}Al NMR spectrum of kyanite obtained with the experiment in Fig. 14b. Three long narrow ridges can be identified (the isotropic shifts are marked with arrows in the F_1 dimension) and, as two of the C_Q values for kyanite are very similar (*14*), these correspond to the four crystallographically inequivalent sites.

DISCUSSION AND CONCLUSIONS

The various methods proposed for obtaining pure absorption-mode lineshapes in MQMAS experiments of half-integer quadrupolar nuclei can be classified according to whether the data are amplitude- or phase-modulated as a function of t_1. Until now, both classes of experiment have most often been performed in such a way that the inhomogeneous quadrupolar broadening is spread out along a ridge which has a slope of $-7/9$ or $19/12$ with respect to the F_2 axis for spin $I = 3/2$ and 5/2, respectively. In this paper we have shown

that there are disadvantages associated with recording the data in this fashion. First, this approach means that the echo that is formed moves through the acquisition period, t_2, as the evolution period, t_1, is incremented, which, in turn, means that the t_2 period is much longer than necessary and that complicated t_1-dependent weighting functions must be used to optimize the sensitivity. Second, it means that, after going to considerable trouble (as usual) to optimize lineshapes, minimize spurious signals, maximize the sensitivity, etc., the spectroscopist has to undo much of this good work by applying a shearing transformation to the final spectrum. This transformation can result in a significant distortion of the two-dimensional lineshapes and, in particular, of the F_2 cross sections containing the individual second-order broadened spectra. Opinions will differ, but it is our strong preference to avoid this last step.

Phase-modulated whole-echo MQMAS experiments yield pure absorption-mode lineshapes when the inhomogeneous quadrupolar broadening is much greater than the homogeneous broadening. In this limit, compared to the amplitude-modulated experiments in Figs. 1a and 9, they have the advantage that only a single coherence transfer pathway need be selected, thereby avoiding the need to use z filters or carefully calibrated single pulses to combine two mirror-image pathways with equal amplitudes. We have introduced phase-modulated split-t_1 experiments where the whole echo is stationary within the acquisition period, t_2 (meaning that the t_2 period is short and that simple weighting functions can be used), and where the inhomogeneously broadened ridges are parallel to F_2, thereby avoiding the need for shearing. In addition to these practical advantages, for spin $I = 3/2$, the inherent sensitivity of the optimum phase-modulated split-t_1 experiment (Fig. 12a) is expected (and, indeed, observed) to be slightly better than that of either the shifted-echo or the shifted-antiecho experiment in Fig. 1b since it features both a short spin-echo interval, τ, and an optimum coherence transfer step of $|\Delta p| = 2$. Finally, we also expect that the sensitivity of the optimum versions of the phase-modulated split-t_1 experiment (Figs. 12a and 14b for spins $I = 3/2$ and 5/2, respectively) will often be better than that of the amplitude-modulated whole-echo experiment, since the latter, despite its theoretical $\sqrt{2}$ sensitivity advantage, requires a longer spin-echo interval, τ, and makes use of a coherence transfer step with $|\Delta p| = 4$.

Amplitude-modulated MQMAS experiments can be used to yield pure absorption-mode lineshapes whatever the ratio of the inhomogeneous to homogeneous broadening. We have introduced amplitude-modulated split-t_1 experiments where the time-domain signal is stationary within the acquisition period, t_2, and where the inhomogeneously broadened ridges are parallel to F_2. In spite of these practical advantages, the sensitivities of the two amplitude-modulated split-t_1 experiments are expected (and observed) to be slightly worse than that of the simple amplitude-modulated experiment in Fig. 1a. This is be-

cause at least one additional pulse is always required. It should be noted, however, that the amplitude-modulated experiments are most clearly preferable to the phase-modulated MQMAS experiments when the inhomogenous broadening is small and that it is in this limit that shearing is least desirable.

In summary, therefore, we have shown that MQMAS experiments that refocus the anisotropic second-order quadrupolar broadening in the evolution period, t_1, have many practical advantages and are well worth considering as alternatives to those experiments that require the application of a shearing transformation to the final spectrum. The sensitivities of split-t_1 MQMAS experiments are comparable to those of the other methods and, in the case of phase-modulated MQMAS experiments for spin $I = 3/2$, are even expected to be slightly superior.

APPENDIX

TABLE A1
Examples of Phase Cycles for Experiments in Fig. 1a

Simple echo experiment (spin $I = 3/2$)
ϕ_1: 0° 30° 60° 90° 120° 150° 180° 210° 240° 270° 300° 330°
ϕ_2: 0°
R_x: 0° 90° 180° 270°
Simple antiecho experiment (spin $I = 3/2$)
ϕ_1: 0° 30° 60° 90° 120° 150° 180° 210° 240° 270° 300° 330°
ϕ_2: 0°
R_x: 0° 270° 180° 90°
Simple amplitude-modulated experiment
ϕ_1: 0° 60° 120° 180° 240° 300° 90° 150° 210° 270° 330° 30°
    180° 240° 300° 0° 60° 120° 270° 330° 30° 90° 150° 210°
ϕ_2: 6(90°) 6(180°) 6(270°) 6(0°)
R_x: 3(0° 180°) 3(90° 270°) 3(180° 0°) 3(270° 90°)

TABLE A2
Examples of Phase Cycles for Experiments in Fig. 1b

Shifted-echo experiment (spin $I = 3/2$)
ϕ_1: 0° 30° 60° 90° 120° 150° 180° 210° 240° 270° 300° 330°
ϕ_2: 0°
ϕ_3: 12(0°) 12(45°) 12(90°) 12(135°)
    12(180°) 12(225°) 12(270°) 12(315°)
R_x: 3(0° 90° 180° 270°) 3(90° 180° 270° 0°)
    3(180° 270° 0° 90°) 3(270° 0° 90° 180°)
Shifted-antiecho experiment (spin $I = 3/2$)
ϕ_1: 0° 30° 60° 90° 120° 150° 180° 210° 240° 270° 300° 330°
ϕ_2: 0°
ϕ_3: 12(0°) 12(45°) 12(90°) 12(135°)
    12(180°) 12(225°) 12(270°) 12(315°)
R_x: 3 (0° 270° 180° 90°) 3(90° 0° 270° 180°)
    3(180° 90° 0° 270°) 3(270° 180° 90° 0°)
Amplitude-modulated whole-echo experiment
ϕ_1: 0° 60° 120° 180° 240° 300°
ϕ_2: 0°
ϕ_3: 6(90°) 6(135°) 6(180°) 6(225°)
    6(270°) 6(315°) 6(0°) 6(45°)
R_x: 3(0° 180°) 3(90° 270°) 3(180° 0°) 3(270° 90°)

TABLE A3
Examples of Phase Cycles for Experiments in Figs. 9 and 14

Amplitude-modulated split-t_1 experiment with z filter
    (spin $I = 3/2$) (Fig. 9a)
ϕ_1: 0° 60° 120° 180° 240° 300°
ϕ_2: 24(0°) 24(90°) 24(180°) 24(270°)
ϕ_3: 0°
ϕ_4: 6(0°) 6(90°) 6(180°) 6(270°)
R_x: 3(0° 180°) 3(90° 270°) 3(180° 0°) 3(270° 90°)
    3(180° 0°)
    3(270° 90°) 3(0° 180°) 3(90° 270°)
Amplitude-modulated split-t_1 experiment (spin $I = 3/2$) (Fig. 9b)
ϕ_1: 4(0° 60° 120° 180° 240° 300°) 4(90° 150° 210° 270° 330° 30°)
    4(180° 240° 300° 0° 60° 120°) 4(270° 330° 30° 90° 150° 210°)
ϕ_2: 6(0°) 6(90°) 6(180°) 6(270°) 6(90°) 6(180°) 6(270°) 6(0°)
    6(180°) 6(270°) 6(0°) 6(90°) 6(270°) 6(0°) 6(90°) 6(180°)
ϕ_3: 24(90°) 24(180°) 24(270°) 24(0°)
R_x: 3(0° 180°) 3(180° 0°) 3(0° 180°) 3(180° 0°)
    3(90° 270°) 3(270° 90°) 3(90° 270°) 3(270° 90°)
    3(180° 0°) 3(0° 180°) 3(180° 0°) 3(0° 180°)
    3(270° 90°) 3(90° 270°) 3(270° 90°) 3(90° 270°)
Amplitude-modulated split-t_1 experiment (spin $I = 5/2$) (Fig. 14a)
ϕ_1: 0° 60° 120° 180° 240° 300°
ϕ_2: 6(0°) 6(45°) 6(90°) 6(135°) 6(180°) 6(225°) 6(270°) 6(315°)
ϕ_3: 90°
R_x: 3(0° 180°) 3(180° 0°)

REFERENCES

1. L. Frydman and J. S. Harwood, *J. Am. Chem. Soc.* **117,** 5367 (1995).

2. C. Fernandez and J. P. Amoureux, *Solid State Nucl. Magn. Reson.* **5,** 315 (1996).

3. C. Fernandez and J. P. Amoureux, *Chem. Phys. Lett.* **242,** 449 (1995).

4. D. Massiot, B. Touzo, D. Trumeau, J. P. Coutures, J. Virlet, P. Florian, and P. J. Grandinetti, *Solid State Nucl. Magn. Reson.* **6,** 73 (1996).

5. A. Medek, J. S. Harwood, and L. Frydman, *J. Am. Chem. Soc.* **117,** 12779 (1995).

6. G. Wu, D. Rovnyak, B. Sun, and R. G. Griffin, *Chem. Phys. Lett.* **249,** 210 (1996).

7. C. Jäger, K. Herzog, B. Thomas, M. Feike, and G. Kunath-Fandrei, *Solid State Nucl. Magn. Reson.* **5,** 51 (1995).

8. C. Fernandez, J. P. Amoureux, L. Delmotte, and H. Kessler, *Microporous Mater.* **6,** 125 (1996).

9. R. E. Youngman, U. Werner-Zwanziger, and J. W. Zwanziger, *Z. Naturforsch. A* **51,** 321 (1996).

10. S. P. Brown, S. J. Heyes, and S. Wimperis, *J. Magn. Reson. A* **119,** 280 (1996).

11. J. V. Hanna, M. E. Smith, and H. J. Whitfield, *J. Am. Chem. Soc.* **118,** 5772 (1996).

12. J. P. Amoureux, C. Fernandez, and L. Frydman, *Chem. Phys. Lett.* **259,** 347 (1996).

13. C. Fernandez, J. P. Amoureux, J. M. Chezeau, L. Delmotte, and H. Kessler, *Microporous Mater.* **6,** 331 (1996).

14. J. H. Baltisberger, Z. Wu, J. F. Stebbins, S. H. Wang, and A. Pines, *J. Am. Chem. Soc.* **118,** 7209 (1996).

15. A. Samoson, *J. Magn. Reson. A* **121,** 209 (1996).

16. G. Wu, D. Rovnyak, and R. G. Griffin, *J. Am. Chem. Soc.* **118,** 9326 (1996).

17. J. Rocha, A. P. Esculas, C. Fernandez, and J. P. Amoureux, *J. Phys. Chem.* **100,** 17889 (1996).

18. D. Massiot, R. Conanec, W. Feldmann, R. Marchand, and Y. Laurent, *Inorg. Chem.* **35,** 4957 (1996).

19. D. Massiot, *J. Magn. Reson. A* **122,** 240 (1996).

20. H. Kraus, R. Prins, and A. P. M. Kentgens, *J. Phys. Chem.* **100,** 16336 (1996).

21. C. Jäger, P. Hartmann, G. Kunath-Fandrei, O. Hirsch, P. Rehak, J. Vogel, M. Feike, H. W. Spiess, K. Herzog, and B. Thomas, *Ber. Bunsenges. Phys. Chem.* **100,** 1560 (1996).

22. J. P. Amoureux, C. Fernandez, and S. Steuernagel, *J. Magn. Reson. A* **123,** 116 (1996).

23. J. Rocha, Z. Lin, C. Fernandez, and J. P. Amoureux, *Chem. Commun.* **22,** 2513 (1996).

24. P. Sarv, C. Fernandez, J. P. Amoureux, and K. Keskinen, *J. Phys. Chem.* **100,** 19223 (1996).

25. S. P. Brown and S. Wimperis, *J. Magn. Reson.* **124,** 279 (1997).

26. E. R. Andrew, *in* ''Encyclopedia of Nuclear Magnetic Resonance'' (D. M. Grant and R. K. Harris, Eds.), Vol. 5, p. 2891, Wiley, Chichester (1996).

27. S. Ganapathy, S. Schramm, and E. Oldfield, *J. Chem. Phys.* **77,** 4360 (1982).

28. A. Samoson, E. Lippmaa, and A. Pines, *Mol. Phys.* **65,** 1013 (1988).

29. A. Llor and J. Virlet, *Chem. Phys. Lett.* **152,** 248 (1988).

30. K. T. Mueller, B. Q. Sun, G. C. Chingas, J. W. Zwanziger, T. Terao, and A. Pines, *J. Magn. Reson.* **86,** 470 (1990).

31. P. J. Grandinetti, J. H. Baltisberger, A. Llor, Y. K. Lee, U. Werner, M. A. Eastman, and A. Pines, *J. Magn. Reson. A* **103,** 72 (1993).

32. S. P. Brown and S. Wimperis, *Chem. Phys. Lett.* **237,** 509 (1995).

33. J. P. Amoureux, *Solid State Nucl. Magn. Reson.* **2,** 83 (1993).

34. R. N. Zare, ''Angular Momentum,'' Chap. 3, Wiley, Chichester (1988).

35. G. Bodenhausen, H. Kogler, and R. R. Ernst, *J. Magn. Reson.* **58,** 370 (1984).

36. A. Wokaun and R. R. Ernst, *J. Chem. Phys.* **67,** 1752 (1977).

37. S. Vega and Y. Naor, *J. Chem. Phys.* **75,** 75 (1981).

38. R. R. Ernst, G. Bodenhausen, and A. Wokaun, ''Principles of Nuclear Magnetic Resonance in One and Two Dimensions,'' Chap. 6, Clarendon Press, Oxford (1987).

39. D. J. States, R. A. Haberkorn, and D. J. Ruben, *J. Magn. Reson.* **48,** 286 (1982).

40. D. Marion and K. Wüthrich, *Biochem. Biophys. Res. Commun.* **113,** 967 (1983).

41. P. T. Callaghan, ''Principles of Nuclear Magnetic Resonance Microscopy,'' Chap. 2, Clarendon Press, Oxford (1987).

42. R. M. Bracewell, ''The Fourier Transform and Its Applications,'' Chap. 6, McGraw–Hill, New York (1987).

43. R. R. Ernst, G. Bodenhausen, and A. Wokaun, ''Principles of Nuclear Magnetic Resonance in One and Two Dimensions,'' Chap. 8, Clarendon Press, Oxford (1987).

44. O. W. Sørensen, M. Rance, and R. R. Ernst, *J. Magn. Reson.* **56,** 527 (1984).